

**POLITECNICO DI TORINO**

Master's Degree in Mechatronic Engineering



**Politecnico  
di Torino**

Master's Degree Thesis

**Design of a permanent-magnet,  
synchronous and limited-angle torque  
motor for a rotary spool valve**

Supervisors

Prof. Nicola AMATI

Prof. Renato GALLUZZI

Dr. Fabio COTTO

Candidate

Alessio TIMI

July 2023



# Summary

This thesis dissertation focuses on the design of a limited angle torque motor capable of driving and controlling a spool valve of a fully active suspension system for automotive applications.

Such a system can operate as a passive and semi-active damper, absorbing and dissipating energy from the interaction between the road and the vehicle, but it is also able to introduce energy into the above equation. This allows the vehicle to achieve better results in terms of both handling and comfort. An example of the improvement in handling is the reduction and eventual elimination of the rolling rotation of the vehicle's chassis during the various phases of a turn, while in terms of comfort, in the event of a bump or hole in the path of a wheel, the system could actively raise or lower the wheel hub, smoothing out the effects of a change in the road on the body of the vehicle.

The motor designed in this paper is an electric motor with permanent magnets mounted on the surface of the rotor and windings powered by a DC current wound around the stator.

The state of the art of this type of motor is not very extensive due to the narrow window of possible applications, so this dissertation aims to develop a possible solution to the suspension problem without the use of a 3-phase excitation and also to study this category of rotary motors in more detail, with the possibility of re-evaluating it and putting it in a better light.

The geometry of the motor is drawn in parametric form to facilitate future modifications and to maintain flexibility for further modifications. Then the dimensions are optimized using the particle swarm algorithm to find the best solutions in terms of torque capacity without exceeding the constraints due to space and the maximum flux that the ferromagnetic cores can withstand.

Although the project did not lead to a successful result for the suspension application, it not only represents a thorough study of the literature on limited angle motors and optimization algorithms, but also shows a flexible MatLab script to design a new limited angle motor for different applications and with new dimensions.

# Acknowledgements

I am writing this letter to express my sincere gratitude and appreciation for the guidance, support, and assistance I received while completing my dissertation. I would like to take this opportunity to acknowledge the invaluable contributions of several individuals and organizations who played an important role in making this research project possible.

First and foremost, I would like to express my sincere appreciation to my supervisors, Renato Galluzzi and Fabio Cotto, for their support, guidance, and valuable insights. Their expertise, dedication, and patience have been instrumental in setting the direction of my work and refining my analytical skills, which has greatly enriched the quality of my dissertation.

I would also like to thank Nicola Amati for the opportunity to work on such a project dealing with a topic of great interest to me, especially given the evolution of my university career.

In addition, I would like to express my gratitude to Way Assauto, which has welcomed me and given me the opportunity to work and implement all the knowledge I have acquired during my studies. I am also deeply grateful to its employees, whom now I have the pleasure to call colleagues, especially Luca Bistolfi, who has accompanied me not only as a tutor but also as a friend.

Finally, the greatest and warmest thanks go to my family and friends for their unwavering love, understanding, and encouragement throughout this challenging and enduring endeavor. Their belief in my abilities and constant motivation were crucial in keeping me focused and determined throughout the various stages of my journey. They celebrated with me after a success and helped me get back on my feet after a defeat. That is worth much more to me than what I can express in words.

Once again, I want to express my deepest gratitude to everyone who has shared a part of this journey with me. Your contributions have had a lasting impact on my personal growth.



# Table of Contents

<b>List of Tables</b>	VII
<b>List of Figures</b>	VIII
<b>1 Introduction and Objectives</b>	<b>1</b>
1.1 Thesis objectives . . . . .	1
1.2 Full active system . . . . .	1
1.2.1 Passive Suspension . . . . .	2
1.2.2 Active suspension . . . . .	4
1.3 Electric motors . . . . .	7
1.3.1 DC motors . . . . .	9
1.3.2 AC motors . . . . .	11
1.4 LATM . . . . .	17
1.4.1 State of the art . . . . .	17
1.4.2 Proposed LATM structure . . . . .	19
1.5 Thesis outline . . . . .	20
<b>2 Pre processor analysis</b>	<b>21</b>
2.1 Parametric geometry . . . . .	22
2.2 Object properties . . . . .	24
2.2.1 Magnet . . . . .	24
2.2.2 Ferromagnetic material . . . . .	26
2.2.3 Armature windings . . . . .	28
2.3 Block properties . . . . .	30
<b>3 Post processor analysis</b>	<b>31</b>
3.1 Modifications on the dimensions of the magnets . . . . .	32
3.1.1 Rotor pole angle arc . . . . .	32
3.1.2 Width of the magnets . . . . .	33
3.2 Modifications on the dimensions of the armature windings . . . . .	33
3.2.1 Air gap (distance between the stator core and PMs) . . . . .	33

3.2.2	Mechanical clearance . . . . .	34
3.2.3	Parameter H . . . . .	34
3.3	Considerations on the simulations . . . . .	36
3.3.1	Hysteresis losses . . . . .	37
3.3.2	Eddy current losses . . . . .	38
3.4	Flux analysis . . . . .	38
<b>4</b>	<b>Parameter optimization</b>	<b>41</b>
4.1	Choice of the optimization algorithm . . . . .	41
4.1.1	Population based algorithms . . . . .	42
4.1.2	Particle swarm optimization . . . . .	44
4.2	Implementation of the algorithm . . . . .	47
<b>5</b>	<b>Results and conclusions</b>	<b>51</b>
5.1	Optimization results . . . . .	52
5.2	Comparisons . . . . .	55
5.2.1	Increased diameter on the same simulation environment . . .	55
5.2.2	LATM from paper [5] . . . . .	57
5.2.3	3-Phase motor . . . . .	59
5.3	Conclusions . . . . .	61
<b>A</b>	<b>MatLab scripts</b>	<b>62</b>
A.1	Function used to compute peak torque and maximum flux . . . . .	62
A.2	Optimization of the parameters with particle swarm algorithm . . .	67
	<b>Bibliography</b>	<b>68</b>

# List of Tables

1.1	Comparison of AC machines . . . . .	14
2.1	Comparison of four PMs . . . . .	24
2.2	Comparison of three typical materials for cores . . . . .	26
4.1	Results of several optimization runs . . . . .	48

# List of Figures

1.1	Suspension . . . . .	2
1.2	Force velocity curve for a passive damper . . . . .	3
1.3	Force velocity curve for a semi-active damper . . . . .	5
1.4	Force velocity regions for an active damper . . . . .	6
1.5	Example of spool and sleeve components of a rotary valve . . . . .	7
1.6	Classification of electric motors . . . . .	9
1.7	Permanent magnet DC motor . . . . .	10
1.8	Brushless DC motor . . . . .	11
1.9	Examples of synchronous machine types . . . . .	12
1.10	Squirrel cage rotor for an IM . . . . .	13
1.11	Wound rotor for an IM . . . . .	13
1.12	3-Phase inverter . . . . .	14
1.13	PN junction . . . . .	15
1.14	Transistor . . . . .	15
1.15	Example of 3-Phase PWM signals and output voltages . . . . .	16
1.16	LATM proposed by Nasiri-Zarandi, Mirsalim and Cavagnino . . . . .	18
1.17	3-D schematic of a four-pole pancake motor . . . . .	18
1.18	Single-phase LATM with cylindrical Halbach . . . . .	19
1.19	Force generated in the single-phase LATM with cylindrical Halbach . . . . .	19
2.1	Parametric geometry of the motor . . . . .	23
2.2	B-H curve of NdFeB magnet . . . . .	25
2.3	B-H curve of M-27 steel . . . . .	27
3.1	Torque-angle characteristic curve with different rotor pole angle arcs . . . . .	32
3.2	Torque-angle characteristic curve with different magnet widths . . . . .	33
3.3	Torque-angle characteristic curve with different air gaps . . . . .	34
3.4	Torque-angle characteristic curve with different mechanical clearances . . . . .	35
3.5	Torque-angle characteristic curve with different values of $H$ . . . . .	35
3.6	Hysteresis loop of a ferromagnetic material . . . . .	36
3.7	Radial lines to estimate flux on the cores . . . . .	39

3.8	Flow chart to pick viable geometries . . . . .	40
4.1	Classification of optimization algorithms . . . . .	42
4.2	Initial position of the swarm . . . . .	46
4.3	Position of the swarm after 5 iterations . . . . .	46
4.4	Position of the swarm after 10 iterations . . . . .	46
4.5	Position of the swarm after 20 iterations . . . . .	46
4.6	Position of the swarm after 50 iterations . . . . .	46
4.7	Position of the swarm after 100 iterations . . . . .	46
4.8	3D distribution of the results of PSO . . . . .	49
5.1	Final version of the geometry with meshes . . . . .	51
5.2	FEA of LATM without stator excitation . . . . .	52
5.3	FEA of LATM with stator excitation . . . . .	53
5.4	Air gap flux density over rotor angle . . . . .	53
5.5	Torque-angle characteristic . . . . .	54
5.6	Torque-current density characteristic . . . . .	54
5.7	Torque-angle characteristic comparison . . . . .	55
5.8	Air gap flux density of the two simulated geometries . . . . .	56
5.9	Torque-angle characteristic curve taken from [5] . . . . .	57
5.10	Torque-angle characteristic with scaled torque . . . . .	58
5.11	Airgap flux density of different geometries simulated and the one taken from the paper . . . . .	58
5.12	3-Phase motor structure taken from the design report . . . . .	59
5.13	Torque-angle characteristic curve of 3-phase motor . . . . .	60
5.14	Air gap flux density of 3-phase motor . . . . .	60



# Chapter 1

## Introduction and Objectives

This work is carried out in collaboration with Way Assauto, a historical Italian company founded in Turin in 1906 and specializing in the design and production of shock absorbers. This project deals with the development of an electric motor that is part of an active suspension system.

### 1.1 Thesis objectives

The objective of this work is to develop an electric motor that drives the spool of a hydraulic valve. They are part of a more complex system, namely an active damper for automotive applications. In the next chapters, a thorough literature review on suspension systems and electric motors will be given. More details about the complete active system are presented later, along with the various design limitations and performance requirements.

The introduction then focuses on the state of the art in LATMs. This is followed by the choice of structure to be designed. Finally, an overview of the entire thesis is provided, concluding the first chapter and shifting the focus to the main body of the thesis.

### 1.2 Full active system

An active suspension system [1] is a type of vehicle suspension in which electronic sensors and actuators control the motion of the suspension system. Unlike a traditional passive suspension system that relies on mechanical springs and dampers to absorb shocks and vibrations, an active suspension system can actively adjust suspension characteristics in response to changing driving conditions and road surfaces.

Active suspension systems can improve vehicle handling, stability, and comfort

by reducing body roll, pitch, and yaw during acceleration, braking, and turning. They can also provide a smoother ride on rough roads or over bumps. An active suspension system's electronic sensors measure the vehicle's motion and send signals to a control unit, which then adjusts hydraulic actuators to change the suspension's stiffness or damping characteristics. The hydraulic actuators are located between the unsprung mass, which consists of the wheel, tire, shaft, and all the components between the suspension and the ground, and the sprung mass, which is the body or chassis.

They can change the position of the suspension in real time to maintain consistent ride height and stability. Active suspension systems are more complex and expensive than passive suspension systems.

### 1.2.1 Passive Suspension

The suspension is a system of components that connects a vehicle to its wheels and allows them to move up and down independently of the vehicle body. It is important for absorbing shocks and vibrations caused by the interaction between tires and the road, in other words, for achieving an optimal balance between handling and comfort. The main components are:

- Bearing components and linkages that allow the rotation of the wheel with respect to the strut and its relative movement with respect to the vehicle body
- Primary elastic elements, such as springs and anti-roll bars that control the vertical displacement of the wheels

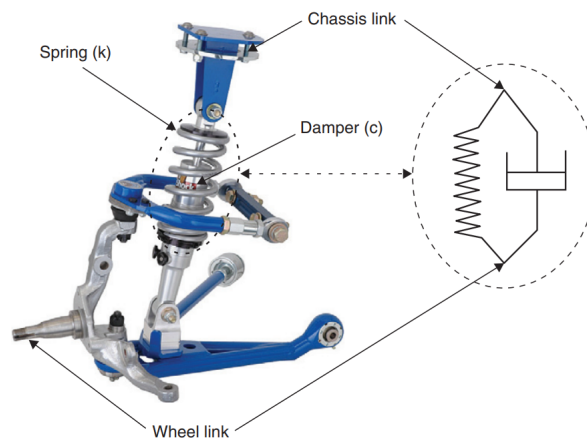


Figure 1.1: Suspension

- Secondary elastic elements, such as rubber bushings attached to the hinges, which act as low-pass filters for frequencies above 30-50 Hz
- Damping element or shock absorber that dissipates the energy stored in the elastic members, reducing body vibrations and peak resonances. It consists of an outer tube connected to the wheel and a piston that moves inside the tube and is connected to the chassis of the vehicle by a rod. The piston divides two chambers and allows the flow of viscous damping fluid through some orifices whose geometry affects the damping coefficient.

Most cars have a passive suspension system that uses mechanical or hydraulic components to absorb and dissipate vibration energy from the vehicle's suspension. The springs store energy when compressed or extended, and the dampers control the rate at which that energy is released. The elastic elements typically used in vehicle suspensions are coil springs or gas springs: coil springs use the elasticity created by the torsion of coils while gas springs rely on the compressibility of gases. Dissipative devices are implemented using hydraulic shock absorbers.

Passive suspensions can be designed to have different elasticity and damping characteristics, depending on the trade-off between ride quality and handling characteristics, but once chosen, they cannot be adapted to different driving conditions. For example, vehicles designed for off-road use typically have soft springs and low damping values, while vehicles designed for high speeds typically have rigid springs with high damping values.

Passive suspension systems have several advantages, including simplicity, low cost,

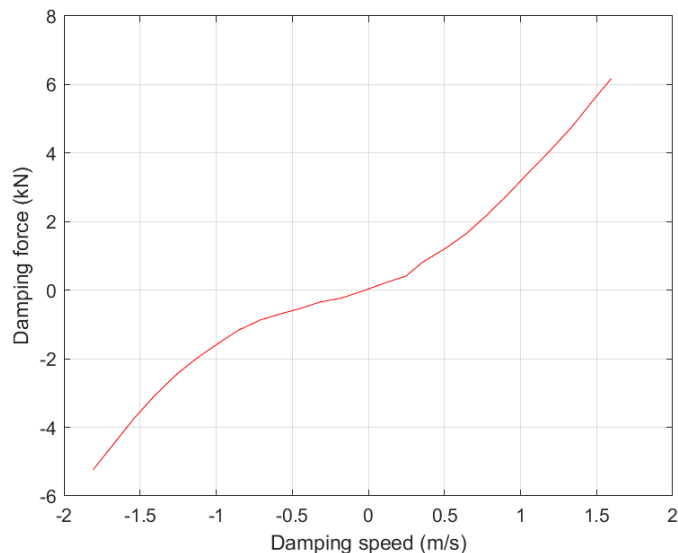


**Figure 1.2:** Force velocity curve for a passive damper

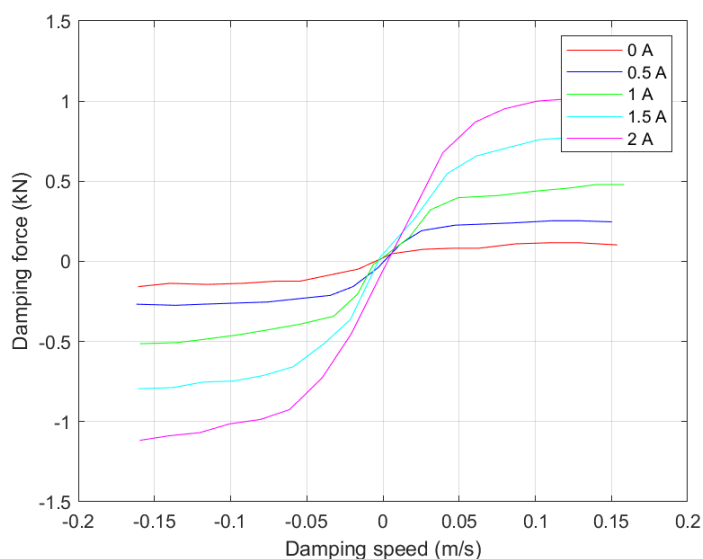
and durability. They are also easy to maintain and repair and do not require an external power source to operate. However, they also have some disadvantages, such as the aforementioned lack of adjustability and control over vehicle handling and stability.

Figure 1.2 shows how the behavior of a passive suspension is limited by the passivity constraint, which, from a mechanical point of view, dictates that the elements in the suspension do not introduce energy into the system, since the elastic elements are only allowed to store the energy transmitted by the road profile, while the damping dissipates it. For this reason, the force-velocity relationship can only occupy the first and third quadrants associated with energy dissipation of energy in the system

## **1.2.2 Active suspension**

Theoretically, different control actions may be introduced depending on the control variables: modulation of the damping force at the dissipative unit level, modulation of the static spring load in response to varying vehicle loads at the elastic unit level, or direct action on the force, replacing both the elastic and damping devices with a force actuator at the full suspension level. Controllable suspensions can be divided into five families:

- Adaptive: the control action is represented by a relatively slow modulation of damping so that the control range is limited by the passivity constraint. It is characterized by a bandwidth of a few hertz and a power demand usually limited to a few watts
- Semi-active: its damping coefficient can be modified by energizing a coil that changes the geometry of the orifices through which the damping oil flows, or by using a magnetorheological fluid that increases its viscosity when exposed to a magnetic field. Overall, the behavior remains passive, but the damper can operate on different working curves. It has a comparatively wide bandwidth (usually about 30–40 Hz), and the power required is relatively low (a few tens of watts)
- Load leveling: they can introduce energy into the system to change the steady state in response to a change in static load. The control acts on the parameter of the springs (usually an air spring). The bandwidth is typically 0.1–1 Hz, but the power requirement is in the range of 100-200 W
- Slow active: the passivity constraint is fully overcome, and power can be injected into the system. The control input is the suspension force  $F$  delivered by an actuator that replaces the passive devices of the suspension. The



**Figure 1.3:** Force velocity curve for a semi-active damper

bandwidth is limited to a few Hertz and the power requirement increases to a few kW

- Fully active: the controlled variable is also the suspension force, but the fully active actuator can respond in milliseconds, resulting in a bandwidth of 20–30 Hz. The available bandwidth is the same as for semi-active suspensions. However, because the range of controllability extends beyond passivity, the total power requirement is much higher and is in the tens of kilowatts

The state-of-the-art in active dampers involves the use of sensors and computer-controlled actuators to continuously adjust the damping forces applied to the suspension. Both hydraulic and electro-mechanical actuators can be used. One of the key challenges in the design of a damper is achieving a balance between comfort and performance. The suspension must be soft enough to absorb bumps and stress from rough roads, but also stiff enough to provide good handling and stability. Some of the latest developments in active dampers include the use of proximity sensors, like lidars, that can detect the road surface ahead and adjust the suspension in anticipation of bumps or rough patches, as well as the use of machine learning algorithms to optimize the suspension settings based on the driving style and conditions.

### Active damper of the project

The system presented in this paper deals with a full-active damper hydraulically actuated by a spool valve that works together with a motor, whose rotor spins

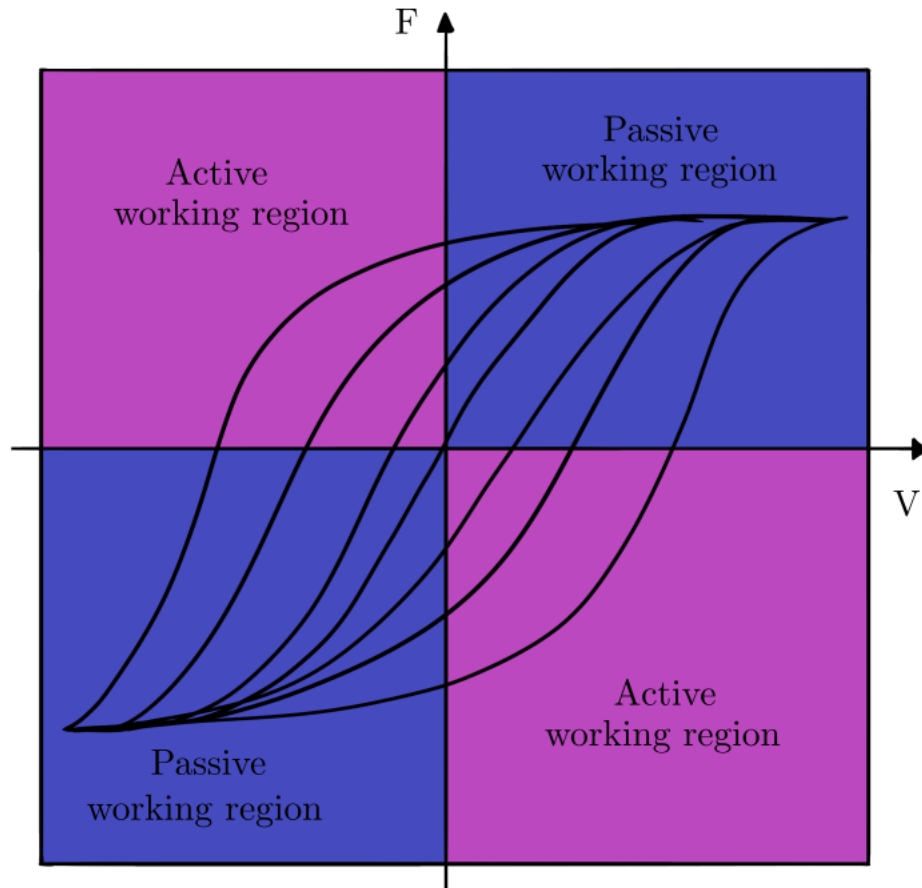


**Figure 1.4:** Force velocity regions for an active damper

simultaneously with the rotary spool inside the sleeve. The spool has been designed with two longitudinal holes fed by both low- and high-pressure damping oil. On the contrary, the sleeve is fixed and has many different ports. The relative position between the spool valve and the sleeve determines the pressure of the fluid passing through the sleeve ports, that feed the two actuator chambers resulting in a pressure gradient that generates a force that tends to move the actuator upwards or downwards.

Moreover, the torquer has some dimension limitations since the whole system has to fit in the narrow space next to the tire that is usually taken up by the passive suspension. The diameter must be smaller than or equal to 60mm and the longitudinal space is 36 mm. It is also required that the motor can develop in a range of motion limited to  $\pm 30^\circ$  a continuous torque of 1 Nm, that is the amount of torque that the motor is able to produce without interruption or failure.

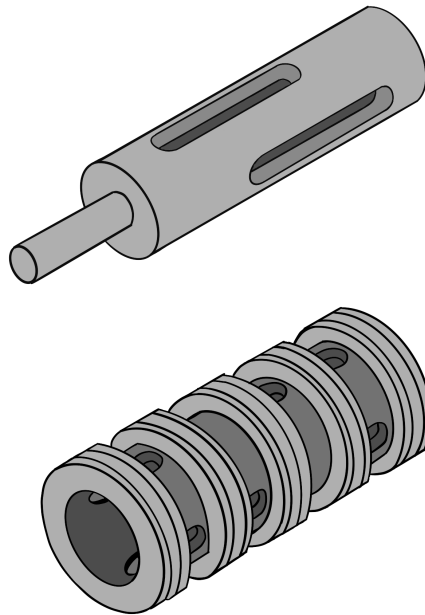


**Figure 1.5:** Example of spool and sleeve components of a rotary valve

It is a parameter used to determine the capacity to perform work and for handling different load conditions.

### 1.3 Electric motors

Electric motors [2] [3] are devices that convert electrical energy into mechanical energy. They work by using electromagnetic fields to create a rotational force, which can be used to power various machines and devices. They are the major alternative solution to internal combustion engines (ICEs). Here are some of the key differences between electric motors and internal combustion engines:

- **Efficiency:** Electric motors are much more efficient than ICEs. While ICEs typically have an efficiency of around 20-30%, electric motors can have efficiencies of up to 95%. This means that electric motors convert a higher percentage of the energy they consume into useful work, while ICEs lose a significant portion of their energy as waste heat
- **Emissions:** Electric motors produce no emissions during operation, while ICEs emit pollutants like carbon monoxide, nitrogen oxides, and particulate matter.

This makes electric motors a cleaner and more environmentally friendly option

- Noise: Electric motors operate quietly, while ICEs can produce significant noise and vibrations
- Maintenance: Electric motors have fewer moving parts than ICEs, which means they require less maintenance and have lower maintenance costs over their lifetimes
- Performance: Electric motors can provide high torque at low speeds, which makes them well-suited for applications that require high levels of torque and precision control. ICEs, on the other hand, typically provide better performance at higher speeds
- Range: Electric motors have limited range compared to ICEs, due to limitations in battery technology. While ICEs can be refueled quickly and easily, electric vehicles require time to recharge their batteries

Overall, electric motors and ICEs have different strengths and weaknesses depending on the application. Electric motors are more efficient, cleaner, and quieter, while ICEs offer better performance at higher speeds and longer ranges. However, the application needs high controllability, and the ability to develop torque at low speed and it needs to be a very compact solution, thus an electric motor is more suitable.

The basic components of an electric motor include a rotor, a stator, and a commutator. The rotor is a rotating part of the motor, while the stator is a stationary part of the motor. Torque is produced by the interaction between the magnetic fields generated by those two components. The stator and rotor have magnetic poles that are arranged to create a rotating magnetic field. When an electric current flows through the stator windings, it generates a magnetic field that interacts with the magnetic field of the rotor. This interaction creates a force that causes the rotor to rotate. The magnitude of the force, and hence the torque produced, depends on the strength of the magnetic fields and the angle between them. The torque produced by an electric motor can be calculated using the following formula:

$$T = k \cdot I \cdot B \cdot \sin \theta \quad (1.1)$$

where  $T$  is the torque produced,  $k$  is a constant that depends on the motor's design,  $I$  is the current flowing through the motor windings,  $B$  is the magnetic field strength, and  $\theta$  is the angle between the stator and rotor magnetic fields.

There are many different types of electric motors, but they can be sorted into two main categories: alternating current (AC) and direct current (DC) motors. How the windings within AC and DC motors interact with each other to produce mechanical force creates further distinctions within each of these classifications.

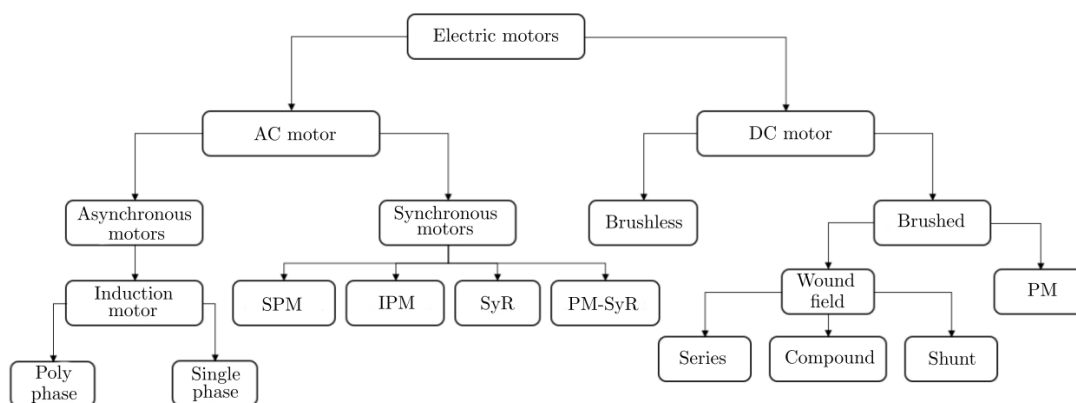


**Figure 1.6:** Classification of electric motors

### 1.3.1 DC motors

These motors can be sorted again into two categories, brushed and brushless, depending on the presence of the mechanical commutator.

#### Brushed motors

The commutator is used in brushed motors to switch the direction of the electrical current flowing through the motor's armature winding at the appropriate time, in order to maintain continuous rotation of the motor shaft. The commutator consists of a set of copper segments, called commutator bars, that are connected to the armature winding and mounted on the motor shaft. A set of brushes, typically made of carbon, are held against the commutator by spring tension and provide a sliding electrical connection as the commutator rotates. As the motor shaft rotates, the brushes make contact with the commutator bars and transfer electrical current to the armature winding. At the same time, the commutator switches the direction of the current flow, so that the magnetic field produced by the armature winding always interacts with the magnetic field produced by the motor's permanent magnets or field winding in the same direction, resulting in a continuous rotation of the motor shaft.

Mechanical commutators have several drawbacks, including the need for frequent maintenance due to wear and arcing between the brushes and commutator bars, which can lead to decreased performance and shorter motor life. They also produce noise and electrical interference, which can be problematic in some applications. There are four main brushed motor types, including:

- Series Motors, with the stator windings in series with the rotor ones, causing their field currents to be identical

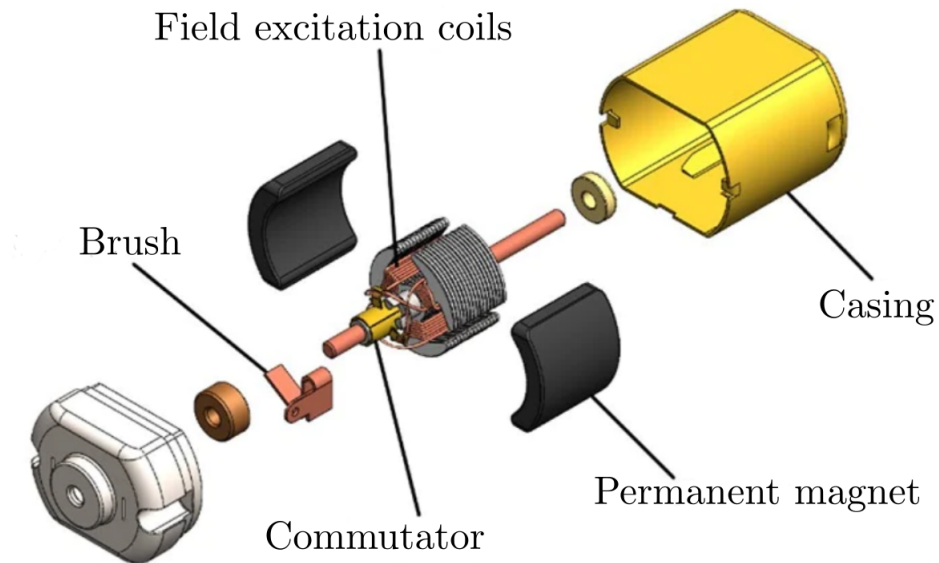


**Figure 1.7:** Permanent magnet DC motor

- Shunt Motors, with the field coil in parallel with the rotor one, making the motor current equal to the sum of the two currents
- Cumulative Compound Motors, combining aspects of both series and shut types, making the motor current equal to the sum of both the series field and shunt field currents
- PMDC Motors, employing permanent magnets

### Brushless motors

Brushless DC motors (BLDCs) perform electronic commutation instead of a mechanical commutator to switch the direction of the current flowing through the motor's windings. In a BLDC motor, the stator contains a series of electromagnets that are arranged in a circular pattern around the rotor. The rotor contains permanent magnets that are magnetized in a specific pattern to interact with the electromagnetic fields created by the stator windings. The electronic controller uses sensors to detect the position of the rotor and sends signals to the stator windings to energize them in the correct sequence and polarity, which generates a rotating magnetic field that drives the rotor. Since there are no brushes or commutator bars in a BLDC motor, there is no physical contact between the rotor and stator, which eliminates the need for maintenance and reduces the likelihood of electrical noise and interference, resulting in better reliability and efficiency and longer life compared to their brushed DC counterparts. BLDC motors also have a higher

power-to-weight ratio and efficiency compared to brushed DC motors, making them ideal for high-performance and reliability applications.

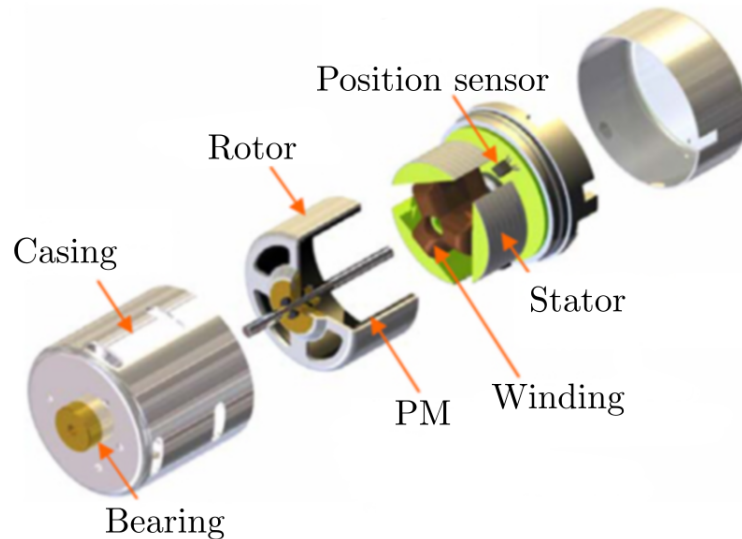


**Figure 1.8:** Brushless DC motor

### 1.3.2 AC motors

This kind of motor can not be supplied just by a battery pack like the previous ones, because it needs an alternating current source, which is obtained by coupling a battery with an inverter. These motors can be sorted into two major categories: synchronous and asynchronous machines.

#### Synchronous machines

The first kind has the rotor speed rigidly related to the AC frequency imposed by the inverter. The rotor design imposes the motor type and name, independently of the stator design and windings type, distributed or concentrated, the main ones are:

- Surface mounted permanent magnet motor(SPM): have PMs mounted on the surface of the rotor. Since the PMs have almost the same magnetic permeability of the air, the reluctance, and so the inductance, computed along any direction is constant making the rotor is isotropic

- Synchronous reluctance motor (SyR): has some flux barriers in the rotor making it highly anisotropic. As a result of this change of inductance along the air gap, the rotor reacts to the stator magnetic field and tends to follow the wave of currents. In other words, the rotor tends to align with the direction of maximum inductance along the magnetic field imposed by the stator, to minimize its magnetic energy
- Internal permanent magnet (IPM): have PMs inserted into the rotor, making the rotor anisotropic, so the torque has both the PMs and SyR components. The main flux component is due to the magnets
- Permanent magnets assisted synchronous reluctance motor (PM-SyR): similar to IPM but the main flux component is due to the reluctance effect

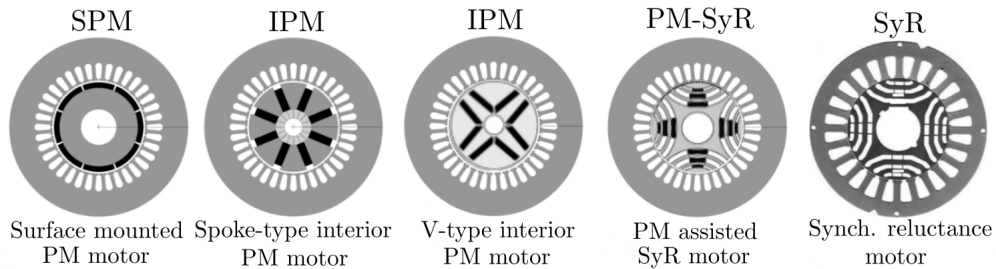


**Figure 1.9:** Examples of synchronous machine types

### Asynchronous machines

Asynchronous motors rely on electromagnetic induction to create a rotating magnetic field that drives the rotor, for this reason, they are also known as induction motors (IM) [4]. They work on the principle of relative motion between a magnetic field and an electrical conductor. When an alternating current is supplied to the stator windings of an asynchronous motor, it creates a rotating magnetic field. The varying nature of the magnetic field induces an electromotive force (EMF) in the rotor windings which produces alternating current, which in turn creates a magnetic field that interacts with the stator field. The interaction of the two fields produces torque, causing the rotor to rotate. The IM rotor can be designed in two ways:

- Squirrel cage, made of a set of conductive bars that are arranged in a cylindrical shape and short-circuited by end rings



**Figure 1.10:** Squirrel cage rotor for an IM

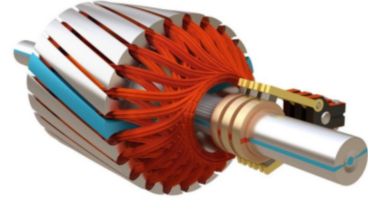


**Figure 1.11:** Wound rotor for an IM

- Wound rotor, made of a set of windings that are connected to slip rings. The slip rings are connected through brushes to an external resistance, which can be used to control the motor's starting torque and speed

The rotor speed is said to be slipping with respect to the AC frequency imposed by the stator,  $f$ :

$$w_m \leq w_s = \frac{2 \cdot \pi \cdot f}{p} \quad (1.2)$$

where  $w_s$  is the synchronous speed and  $p$  is the number of pole pairs. The rotor tends to synchronize to the excitation field but the synchronization is true only with zero torque condition, or no-load condition. The slip is defined as:

$$s = \frac{w_s - w_m}{w_s} \quad (1.3)$$

Nominal slip at rated torque is usually in the range of 3-5%.

### Stator design

A stator for AC machines can be used for both synchronous and asynchronous motors without modifications. However, there are two possible designs regarding windings layout: concentrated and distributed windings. The two winding configurations produce slightly different magnetic fields. Distributed windings produce a nearly sinusoidal field distribution at the airgap, however, they have higher manufacturing costs and longer end-windings. They need more material, resulting in greater Joule losses and increased axial length. On the other hand, concentrated windings are cheaper but they produce harmonics fields. Thus, the excitation field is more distorted affecting the motion of the rotor as well.

	Asynchronous motors		Synchronous motors			
	Squirrel cage	Wound rotor	SPM	IPM	PM-SyR	SyR
Cost	Low	Medium-high	High	Medium	Medium-low	Low
T density	Medium-high	Medium-high	Very high	High	Medium-high	Medium
Anisotropy	No	No	No	Low	High	High
PM	No	No	High	High	Low	No

**Table 1.1:** Comparison of AC machines

### Inverter

As previously mentioned, AC machines must be supplied by a 3-phase inverter. The basic principle behind an inverter is to convert the DC voltage from the input source into an AC voltage waveform that closely approximates a sine wave, for this reason, the inverter is usually called a DC-AC component. The inverter circuit consists of a DC power source, switching devices (transistors or thyristors), and an output filter. The output waveform of an inverter is a series of pulses with varying widths and frequencies that are filtered to produce a smooth AC output waveform. These series of pulses are created in a specific pattern by turning on and off the switching devices. The frequency and duration of these pulses determine the frequency and amplitude of the output AC waveform.

The working principle of a transistor is based on the PN junction, which is a

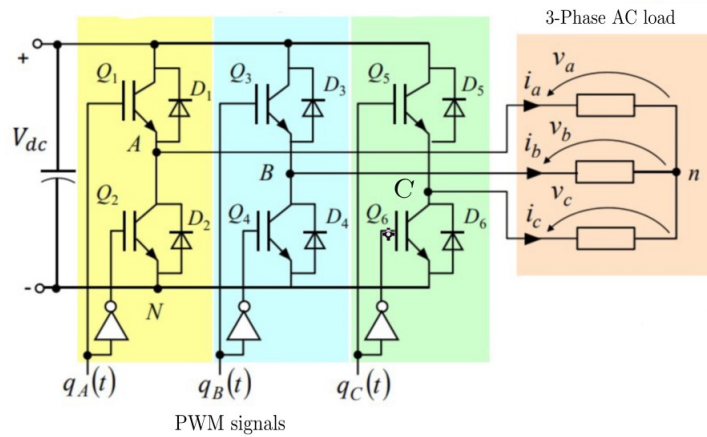


**Figure 1.12:** 3-Phase inverter

type of semiconductor junction formed by bringing together a P-type, positive,

and an N-type, negative, semiconductor material. The P-type material has an excess of holes, positive charge carriers, while the N-type material has an excess of electrons, negative charge carriers. When the two types of materials are brought together to form a PN junction, the holes, and electrons diffuse across the junction and combine, creating a depletion region. The depletion region is a region near the junction where there are no charge carriers of any type. The reason for this is that the electrons in the N-type material near the junction are attracted to the positively charged holes in the P-type material, and the holes in the P-type material are attracted to the negatively charged electrons in the N-type material. This results in a region where there are no free-charge carriers. When a voltage is applied to the PN junction in the forward bias configuration, the depletion region becomes thinner and the flow of current through the junction is increased. This is because the voltage applied to the junction opposes the built-in voltage of the junction, reducing the size of the depletion region and allowing current to flow. On the other hand, when a voltage is applied to the PN junction in the reverse bias configuration, the depletion region becomes wider and the flow of current through the junction is reduced. This is because the voltage applied to the junction reinforces the built-in voltage of the junction, increasing the size of the depletion region and preventing current from flowing. A transistor is a semiconductor device used to amplify or switch electronic signals.

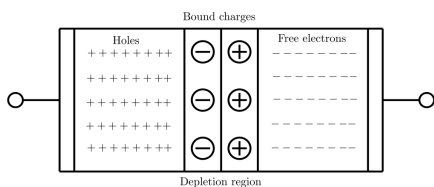


**Figure 1.13:** PN junction

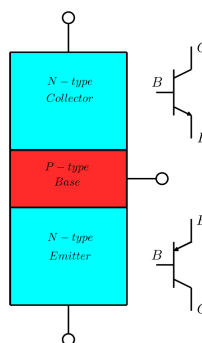


**Figure 1.14:** Transistor

It consists of three layers of material, N-type and P-type semiconductors, forming a sandwich-like structure, resulting in either a PNP or an NPN junction. The transistor has three regions, the emitter, the base, and the collector. The base is located between the emitter and the collector and is very thin compared to the other two regions. The working principle of a transistor is based on the control of the flow of electrons through the transistor by applying a voltage to the base. With the application of an appropriate voltage to the base, the depletion layer becomes thinner and the transistor becomes a closed switch.

The technique of opening and closing the switching devices is called pulse width modulation (PWM). It aims to control the amount of power delivered to a load by rapidly switching a signal on and off. The signal is typically composed of two parts: the carrier waveform and the modulating waveform, or trace. The carrier waveform is a high-frequency, constant-amplitude waveform that serves as the basis for the PWM signal. The modulating waveform is a low-frequency, variable-amplitude waveform that is used to control the width of the pulses in the carrier waveform. The carrier waveform is typically a square wave or a triangular wave with a frequency that is much higher than the frequency of the trace. The high frequency ensures that the output of the PWM signal is continuous and smooth. The trace is used to control the width of the pulses in the carrier. The modulating signal can have any type of waveform, such as a sine wave, square wave, or ramp waveform. The amplitude of the modulating waveform determines the duty cycle of the PWM signal, which is the percentage of time that the carrier signal is on during each cycle. The PWM signal is created by comparing the trace with the carrier. The combination of the two waveforms produces a PWM signal with a frequency that is equal to the frequency of the carrier and a varying duty cycle that is determined by the amplitude of the trace. The output filter of an inverter is

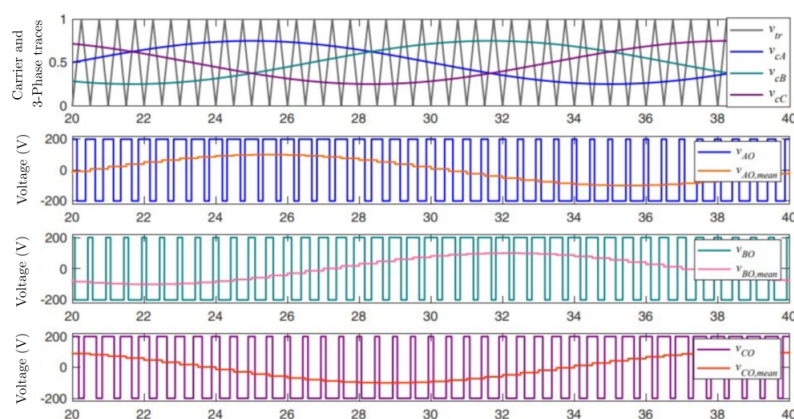


**Figure 1.15:** Example of 3-Phase PWM signals and output voltages

used to remove the high-frequency components of the pulse waveform and smooth the output waveform to a more sinusoidal shape. The filter typically consists of an inductor and capacitor network that attenuates the high-frequency components of the pulse waveform.

## **1.4 LATM**

Another possible electric motor design is the limited angle torque motor (LATM). This motor is an electromechanical actuator specifically designed to provide high torque output over a limited range of motion. This type of motor is commonly used in applications where precise and powerful rotational motion is required within a small angle of rotation, such as in robotics, automation systems, and medical devices. LATMs typically consist of a stator and rotor, with the rotor being designed to rotate within a limited range of motion, usually within  $\pm 90^\circ$ . The stator is typically wound with multiple coils, which are energized to generate the rotating magnetic field required for the rotor to turn. This design provides high torque output over a limited range of motion, which makes it ideal for applications that require precise rotational motion in a small space.

### **1.4.1 State of the art**

The following literature review is conducted on papers and research published on IEEE which is one of the most important technical professional organizations, providing a wide range of quality publications that make the exchange of technical knowledge and information possible among technology professionals.

The solution proposed by Nasiri-Zarandi, Mirsalim, and Cavagnino in [5] is an LATM with a slotless stator with two series-connected armatures toroidally wound around it and two rare-earth permanent magnets (PMs) with high flux densities are mounted on the rotor. Regarding the choice of the magnets, a neodymium magnet is employed because of its high energy and coercive force, which gives the advantages of great peak torque, allowing large air gaps, low weight, and physical size, and low cost. They proposed a new rotor structure where the magnets mounted on the surface are a determined number of bar-type PMs glued together with an adhesive material, rather than one arc-type PM. This solution considerably reduces manufacturing costs at the price of slightly worse performances.

Parham, Hekmati, and Mojtaba Mirsalim presented in [6] a motor that is much different compared to the previous because the flux is axial, rather than radial. These torquers are called pancake motors or flat motors, because of the flat, disc-like shape that characterizes the rotor and stator. This axial flux e-motor has a laminated ferromagnetic slotless stator with a trapezoidal cross-section around which distributed toroidal armature are wound to produce 4 poles. On both sides of the stator, there is a solid disk-shaped ferromagnetic rotor with PMs mounted on the surface to produce an excitation field. The magnetic field generated by the coils is parallel to the axis of rotation, which means that the magnetic flux lines are axial in orientation. In terms of performance, pancake motors have lower efficiency and higher cogging torque than radial flux e-motors, on the other hand, they have

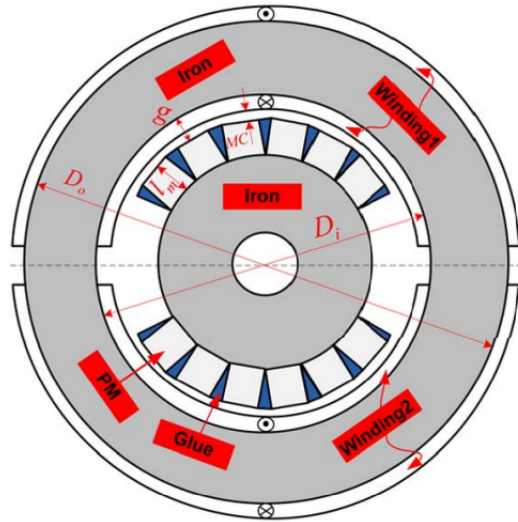


**Figure 1.16:** LATM proposed by Nasiri-Zarandi, Mirsalim and Cavagnino

a simpler design and are easier to manufacture.

In the paper [7], Murali Krishna and Kannan compare two different stator designs,

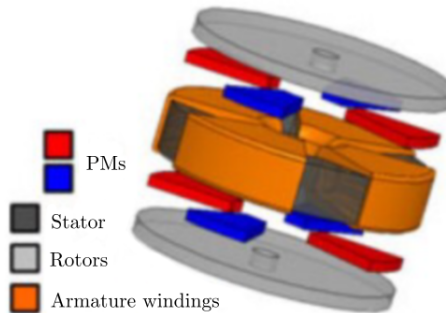


**Figure 1.17:** 3-D schematic of a four-pole pancake motor

slotted and toroidally wound armature. The slotted design has some slots cut in the laminated core, where the armature windings are embedded. On the contrary, the toroidal design has a slotless laminated core around which the wire is directly wound. The slotted design is characterized by a higher torque constant and it performs much better in terms of heat dissipation, on the other hand, it exhibits greater magnetic friction and iron losses. One of the main advantages of the toroidally wound design is the strong reduction in torque ripple since the cogging effect is essentially null for this kind of stator design, which also needs to be encapsulated by epoxy resin to prevent damage and provide rigidity. Regarding the rotor, they

employed samarium cobalt magnets, that feature greater peak torque capability, long-term stability, high resistance to demagnetization, low time constant, and allow large air gaps between stator and rotor.

The paper [8] presents a different approach to the movement on a limited angle. The motor presented consists of a cylindrical Halbach array stator and a moving coil rotor. The array just mentioned is formed by connecting a series of PM segments to form a circle and each segment has its magnetization direction. This solution gives an ideal uniform flux across the air gap and prevents any magnetic flux leakage toward the outside of the motor. The major drawback of this solution is the lack of adjustability of the field excitation which is fixed. The rotor is made of an air-core coil which is energized with a DC excitation. This novel solution manages to achieve a great peak torque keeping the motor compact but has the major disadvantage of a steep torque angle characteristic curve. The torquer develops the peak torque in the neutral position ( $0^\circ$ ) and is unable to produce torque at  $\pm 90^\circ$  from that position. This motor relies on the Lorentz force that has a direct dependence on the cosine of the angle between the coil and its neutral position.

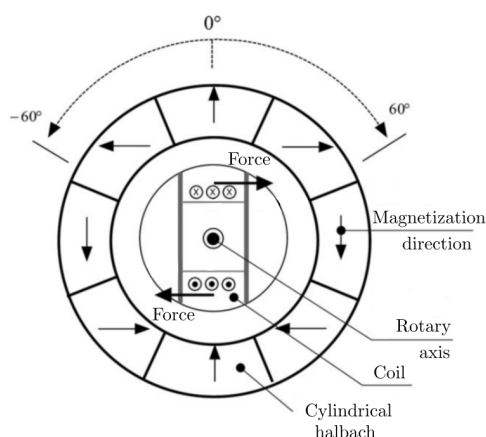


**Figure 1.18:** Single-phase LATM with cylindrical Halbach

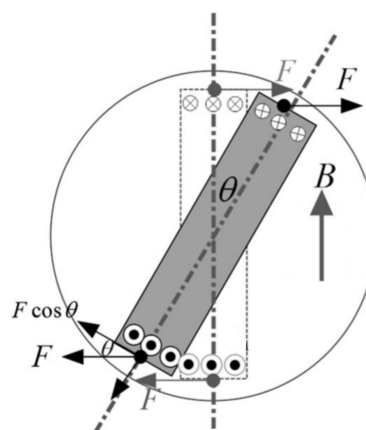


**Figure 1.19:** Force generated in the single-phase LATM with cylindrical Halbach

### 1.4.2 Proposed LATM structure

Limited angle torque motors are suitable for applications where precise control of angular position or torque is required, such as in optical scanning systems or direct laser mirrors, servo-valves or flow control, position missile-guidance radar antennas,

or even open shutters for heat-seeking sensors. They basically can power every system that needs to rotate over small angles. This ability to cover small angles with a continuous motion and high precision makes it a highly suitable option for this project, rather than other types of motors like stepper motors, whose shafts can only move to a finite number of positions. For this reason, the latter is widely implemented in computer numerical control (CNC) machines such as 3D printers. They are also referred to as AC solutions to simplify the overall structure and electronic circuitry.

The structure proposed in the first paper reported is a good starting point for the development of this thesis project. Two series-connected armatures of toroidal windings are picked in combination with the slotless stator for their simplicity of mount and absence of a cogging effect. The Halbach array solution is discarded because of its greater manufacturing cost. The rotor is chosen to have two rare-earth PMs with high flux densities mounted on the surface of the rotor. The employment of electronic commutation rather than mechanical brushes to control the flow of current through the motor offer several advantages, including improved reliability, longer life, and reduced maintenance requirements. The overall structure has other important features like high efficiency, accurate position capability, and high torque and power density.

## **1.5 Thesis outline**

Following this introductory chapter, this thesis project dissertation is organized in this manner:

1. Pre-processor analysis: Design of the parametric geometry of the section of the LATM and subsequent choice of the best materials suitable for the purposes
2. Post processor analysis: Electromagnetic analysis of the geometry developed
3. Optimization of the motor parameters: Different optimization methods are taken into consideration, evaluating the advantages and disadvantages of each one. The fittest algorithm is chosen to define the best geometry, that is the one who develops the greatest torque without exceeding the flux limitations on the two ferromagnetic cores.
4. Results, comparison and conclusions

## Chapter 2

# Pre processor analysis

Considering the future electromagnetic analysis, the finite element method (FEM) and the magnetic equivalent circuit (MEC) are considered possible approaches to the problem.

FEM is a numerical method used to solve partial differential equations (PDEs). It is often employed to model and analyze a wide range of physical systems, including structural mechanics, heat transfer, fluid dynamics, and electromagnetism. Its working principle is based on dividing a complex system into smaller, simpler elements, and solving the equations for each element.

On the other hand, MEC approaches the problem from a different perspective. It uses a circuit-based approach to represent the electromagnetic properties of a system, such as inductance, resistance, and capacitance. It is often used to analyze systems that have a simple geometry and can provide a good approximation of the system's behavior, but it does not provide detailed information about the electromagnetic field distribution.

Even if it is time-consuming and computationally intensive, FEM is preferred to the simpler and faster MEC because of the high precision results when taking into consideration the complex motor geometry and material properties, such as iron saturation and PM characteristics.

The design of the motor is carried out on MatLab interfaced with FEMM through the toolbox OctaveFEMM. FEMM is a suite of programs for solving low-frequency electromagnetic problems on two-dimensional planar and axisymmetric domains. The program addresses both linear and nonlinear magnetostatic, time-harmonic magnetic, linear electrostatic, and steady-state heat flow problems. FEMM [9] is structured as follows:

- Interactive shell ("femm.exe"): multiple document interface pre-processor and post-processor for the various types of problems that FEMM can solve. It contains a computer-aided design (CAD) interface for laying out the geometry

of the problem to be solved and for defining material properties and boundary conditions. It can display field solutions in the form of contour and density plots, also allowing the inspection of the field at arbitrary points, as well as the evaluation of several different integrals and the plot of various quantities of interest along user-defined contours

- "Triangle.exe": covers a vital part of the finite element process, breaking down the solution region into a large number of triangles, which can be increased or decreased to make the solution more or less precise. A larger number of triangles would make their dimension smaller, resulting in a more precise analysis at the cost of a larger computational weight. A trade-off between the two is advised
- Solvers ("fkern.exe" for magnetics; "belasolv" for electrostatics; "hsolv" for heat flow problems; "csolv" for current flow problems): each solver takes a set of data files that describe the problem and solves the relevant PDEs to obtain values for the desired field throughout the solution domain

The software only needs a cross-section of the motor and the specification of the material's properties to evaluate the performance and perform the electromagnetic analysis.

## 2.1 Parametric geometry

The first task is to draw the geometry of the motor, which is made up of the rotor, the moving part, which comprehends the ferromagnetic core and its surface-mounted permanent magnets (PMs), and the stator, the fixed part, composed of another ferromagnetic core and its toroidally wound armature windings.

The geometry is sketched in parametric form to ease future changes due to the optimization. The parameters are:

- $R_{so}$  = stator ferromagnetic core outer radius
- $R_{si}$  = stator ferromagnetic core inner radius
- $R_{ri}$  = rotor ferromagnetic core inner radius
- $MC$  = mechanical clearance (or the distance between windings and PMs)
- $H$  = distance between the end of the windings and the horizontal axis of symmetry of the motor section
- $\theta_R$  = rotor pole angle arc

- $G$  = air gap (or the distance between the stator core and PMs)
- $LM$  = PMs thickness
- $D$  = depth or length of the motor
- $R_{ro}$  = rotor ferromagnetic core outer radius ( $= R_{si} - G - LM$ )
- $WT$  = windings thickness ( $= G - MC$ )

The functions “mi\_addnode” and “mi\_addarc” are used respectively to add nodes and connect them with an arc. The combination of the above functions is used to build the two metal cores, which are circular crowns from a geometric point of view. The function “mi\_addsegment” is required in addition to the previous ones to build the windings and the magnets since their shape are respectively circular crown segment and sector.

The last part of the geometry is the definition of the air gap that is made by two concentric circumferences located between the inner windings and the PMs. It is needed to perform the electromagnetic analysis at different rotor positions.

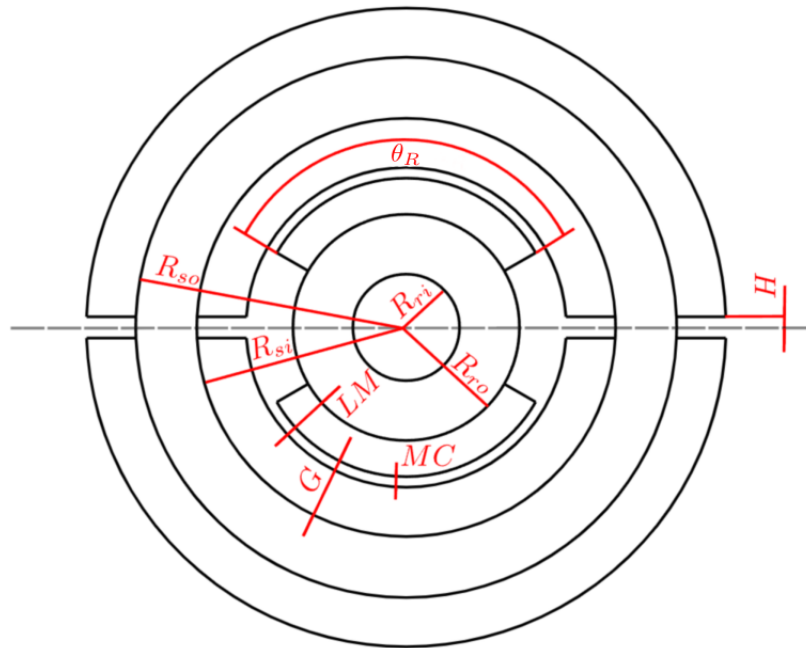


**Figure 2.1:** Parametric geometry of the motor

## 2.2 Object properties

The second step is the definition of the materials and the circuit properties. The materials involved in the motor are air, a rare earth element-based material for the magnet, a ferromagnetic material for the cores, and the wire for the armatures.

### 2.2.1 Magnet

Several important characteristics of magnets are relevant to their use in electric motors, the main ones are:

- Magnetic field strength: the amount of magnetic force a magnet can generate, usually measured in units of Gauss or Tesla. The stronger the magnetic field, the more energy the magnet can produce
- Energy density: the amount of magnetic energy a magnet can produce for a given volume. Magnets with a high energy density can generate a strong magnetic field in a small space, making them more efficient in electric motors
- Temperature tolerance: the ability of a magnet to retain its magnetic properties at high temperatures
- Corrosion resistance: the ability of a magnet to resist corrosion is important to ensure long-term performance in electric motors, as corrosion can weaken or destroy the magnet over time
- Mechanical properties: brittleness and machinability, among others, can affect the ease and cost of manufacturing electric motors that use that magnet
- Cost: an important factor in the overall cost of an electric motor

Magnetic material	Residual flux, $B_r$ (T)	Coercive force, $H_c$ (kA/m)	$BH_{max}$ ( $\text{kJ}/\text{m}^3$ )	Maximum operating temperature ( $^{\circ}\text{C}$ )	Density ( $\text{g}/\text{cm}^3$ )
Ferrite	0.400	295	29	250	4.9
Alnico	1.070	50	40	500	7.3
SmCo	0.920	705	170	250	8.4
NdFeB	1.150	840	240	150	7.4

**Table 2.1:** Comparison of four PMs

The most commonly used magnets in electric motors are hard ferrite, alnico, samarium cobalt (SmCo), and neodymium–ferrite–boron (NdFeB) [10]. Ferrite-based

magnets have a discrete coercivity force and residual flux, which are respectively the intersections of the BH curve with the x- and y-axes.

They also have good temperature resistance while being the lightest material presented in the table. Similarly, alnico magnets have a low maximum of the product of the magnetic flux and magnetic intensity ( $BH_{max}$ ). On the other hand, they combine great residual flux, extremely low coercivity force, and can withstand  $500^{\circ}\text{C}$ . Samarium-cobalt magnets have good properties in every aspect analyzed and for this reason, are often used in high-performance applications such as electric vehicles and aerospace. NdFeB magnets have a high energy density and are relatively inexpensive compared to the previous one, making them a popular choice for many applications. Furthermore, NdFeB permanent magnets give the significant advantages of greater peak torque, higher energy product allowing a smaller physical dimension, higher coercive force, allowing larger air gap, less weight, and less energy cost compared to the other magnets presented. Regarding their mechanical properties, they can be easily machined and shaped but can be brittle and crack or chip if impacted or dropped. Taking into account their significant corrosion problem when exposed to moisture or other damaging agents, it is strongly advised the application a protective coating commonly made of Nickel, Zinc, or Epoxy. Neodymium-iron-boron magnets can withstand the lowest temperature among the presented materials, but considering all the above strengths and weaknesses and also the application, NdFeB magnets are the fittest to the project, especially for their ability to develop greater torque at smaller dimensions.

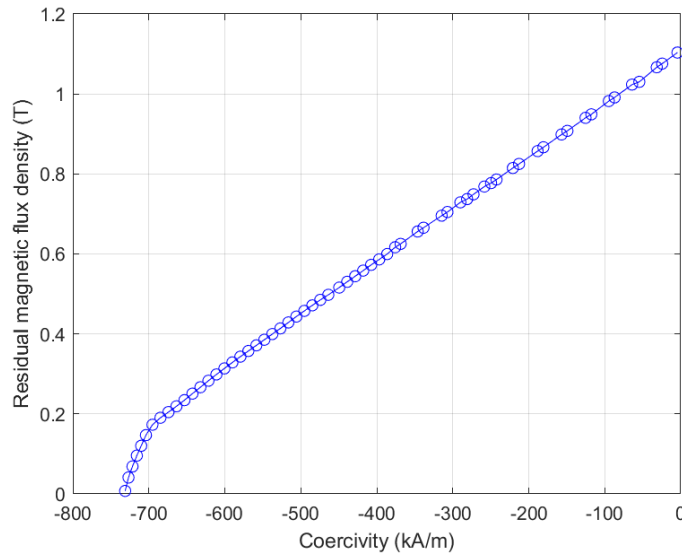


**Figure 2.2:** B-H curve of NdFeB magnet

## 2.2.2 Ferromagnetic material

In general, a good ferromagnetic material candidate for the rotor and stator cores must have low hysteresis loss, low core cavity, and low retentivity. Aside from hysteresis and coercivity, the saturation value of the flux density of the material is also noticeably important as well as the cost. For the choice of material, the main factors taken into account are:

- Magnetic permeability: directly proportional to the material's ability to support the formation of a magnetic field, hence to withstand a greater torque
- Electrical conductivity: low electrical conductivity would reduce eddy current losses, improving the overall efficiency
- Thermal conductivity: good thermal conductivity helps to dissipate heat generated during work
- Mechanical properties: high strength and good dimensional stability are needed to withstand the mechanical stress of operations
- Cost: like magnets, an important factor in the overall cost of an electric motor
- Operating conditions: the material should be able to withstand the operating conditions of the motor, such as temperature, humidity, and vibration

Among the materials presented the alloy made of iron and cobalt yields the best properties, having great permeability and saturation, and maintaining low hysteresis losses, but has the major drawback of being extremely expensive compared to the other two materials.

It has to be considered that the values presented in the table are an estimate because they are strongly dependent on the chemical composition of the alloy. Among the other two, steel is chosen for its low electrical conductivity achieved through some particular manufacturing processes.

Material	Permeability (mH/m)	Hysteresis loss (Ergs per cc per cycle)	Maximum induction (kG)	Coercive force (Oe)	Saturation value (kG)
Steel	5.0	1600	10	0.46	20.5
Iron	6.3	2700	10	1.00	21.4
Fe-Co alloy	23	1500	21	0.23	24

**Table 2.2:** Comparison of three typical materials for cores

Non-oriented electrical steel, also known as non-grain-oriented electrical steel (NGOES) or non-oriented silicon steel, is a type of electrical steel that has been processed to have isotropic magnetic properties, which means consistent magnetic properties regardless of the direction of the magnetic field. This is done by controlling the crystal orientation of the steel during the manufacturing process so that the steel has a random orientation of the grains rather than a preferred orientation. On the other hand, grain-oriented electrical steel (GOES) is processed to have the highest magnetic properties in a specific direction, yielding a highly anisotropic behavior.

The term "fully processed" used to describe electrical steel, refers to a type of steel that has undergone all the necessary processing steps to be ready for use in an electric motor or transformer as presented in [11]. This typically includes cold rolling, annealing, and coating. This production process for NGOES usually begins with hot-rolled steel coils, which are then cold-rolled to reduce the thickness and improve the surface finish. The cold-rolled steel is then annealed to soften the steel and improve its magnetic properties. Annealing is done by heating the steel to a high temperature and then slowly cooling it to room temperature. After annealing, the steel is coated with a thin layer of insulation to prevent the flow of eddy currents within the steel. The coating is typically made of a material such as aluminum, which is applied by a process called electrolytic coating. The steel is then ready to be cut into sheets of the desired size and shape.

NGOES is less expensive and more readily available than GOES and is suitable for use in a wide range of electrical equipment. However, it has lower magnetic

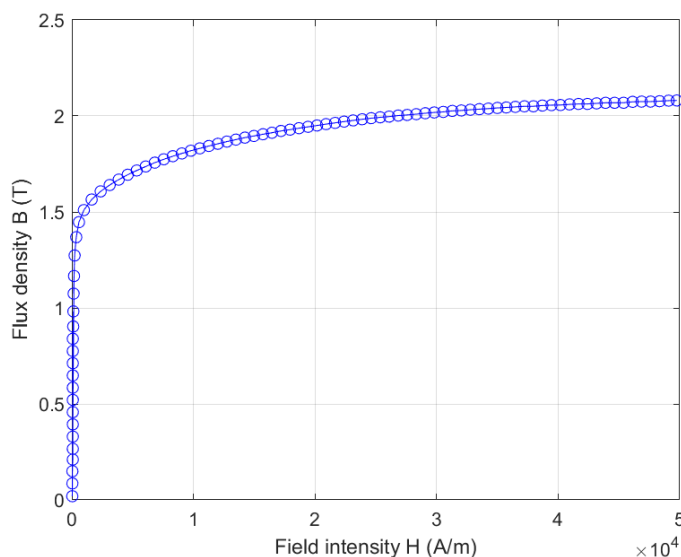


**Figure 2.3:** B-H curve of M-27 steel

properties than GOES, which makes it less efficient and less suitable for use in high-performance applications such as wind turbines and high-efficiency motors. Despite the lower efficiency, fully processed non-oriented electrical steel is the chosen material because of the isotropic magnetic properties, the lower cost, and the ready availability.

The feature “mi\_getmaterial” is used to add a material present in the software database to the system materials library. In this way “N35”, “Air” and “M-27” are added to the library. Regarding the magnet, the "N" refers to its neodymium content, while "35" refers to its maximum energy product, which is a measure of the magnet's strength, in this case, the maximum energy product is 35 mega-gauss-oersteds (MGOe). “M-27” is the nomenclature given to this specific type of alloy steel by the American Iron and steel institute (AISI).

### 2.2.3 Armature windings

Furthermore, “mi\_addmaterial” allows generating a new material from scratch only defining its properties. It is used to generate the windings material, defining their relative permeability in the two axes,  $\mu_x$  and  $\mu_y$ , permanent magnet coercivity,  $H_c$ , and the applied source current density,  $J$ .

The definition of these parameters is directly dependent on the choice of the material for the windings. The most used materials [12] are:

- Copper: the most used material for motor winding construction, primarily due to its high electrical conductivity and relatively low cost. It is typically used with a very thin enamel coating to prevent short circuits from occurring and extends the longevity and efficiency of the wire. The major drawback of this material is its high density making it not the ideal choice for lightweight applications
- Aluminum: compared to copper it is not as common, and has a much lower density, for this reason, it is a better choice in applications where the weight is critical. However, it has a lower electrical conductivity than copper, which has to be compensated using a wire with a larger cross-section to offer the same conductance and power outputs, resulting in a greater volume
- Silver: has the greatest electrical conductivity among any material and also a good corrosion resistance but its price is extremely greater than the others presented

The material chosen is copper for its good properties, cheap price, and ready availability. It has a relative permeability of 0.999994, which is very similar to the permeability of air. For simplicity,  $\mu$  is set to 1 on both axes. Coercivity is a

measure of the resistance of a magnet to having its magnetic field demagnetized, so it is a characteristic of magnetic materials, since copper is a paramagnetic material this parameter is set to 0.

The next feature to define is the applied source current density. The maximum current density in a wire depends on a variety of factors, including the wire's material, cross-sectional area, and temperature. The maximum recommended current density should always be at most  $95MA/m^2$  regardless of wire thickness, but it is usually below  $10MA/m^2$ . It also has to be considered the fill factor, which is a measure of how much of the available space within the winding is occupied by conductor material. It is defined as the ratio of the actual conductor material present in the winding to the total available space within the winding. In general, it ranges from about 60% to 80%. Then in this case it must be considered that the wire cannot precisely fill the circular crown segment previously drawn. For simplicity, this factor is computed as the ratio between the area of a circle and the square circumscribed around it.

$$\frac{A_{circle}}{A_{square}} = \frac{\pi r^2}{4r^2} = \frac{\pi}{4} = 0.78 = 78\% \quad (2.1)$$

Therefore, starting from the initial admissible value of  $8MA/m^2$  and considering the worst case, the final value of current density is computed as:

$$J_{max} = 8MA/m^2 \cdot 0.78 \cdot 0.6 = 3.744MA/m^2 \quad (2.2)$$

For safety reasons, a value of  $J = 3.6MA/m^2$  is chosen.

Moreover, the inner and outer windings have different areas, but they must have the same total current passing through. Since the inner ones have a smaller surface, they represent the critical point. For this reason, the above value of current density is applied only to the inner windings, while for the outer ones it must be rescaled with the following ratio:

$$IWOW = \frac{inner\_windings\_area}{outer\_windings\_area} \quad (2.3)$$

Finally, the sign of the current in the windings must be anti-symmetric with respect to the symmetry plane of the motor, so 4 different materials are defined:

- “25 AWG I+” with  $J = 3.6MA/m^2$  for the inner windings in the lower half
- “25 AWG I-” with  $J = -3.6MA/m^2$  for the inner windings in the upper half
- “25 AWG O+” with  $J = IWOW * 3.6MA/m^2$  for the outer windings in the upper half
- “25 AWG O-” with  $J = -IWOW * 3.6MA/m^2$  for the outer windings in the lower half

## 2.3 Block properties

The following step involves the assignment of a block property to each of the areas initially drawn. The functions “mi\_addblocklabel” and “mi\_selectlabel” both need the coordinates of a point as input to add a label and then select it. Later “mi\_setblockprop” is used to assign one of the materials present in the library to an area. It needs as inputs the block name, the ‘automesh’ set to 1 to let the mesher automatically choose the mesh density, the ‘meshsize’ set to 0 to avoid setting any size constraints, the ‘incircuit’ property defined as ‘none’ since there are circuit properties, the ‘magdir’ for magnetization direction, ‘group’ to add the block to a certain group to facilitate possible further analysis and the ‘turns’ for the number of turns in a coil. The ‘magdir’ element is set to ‘theta’ in the upper PM and ‘theta+180’ in the lower one to give them a radial magnetization direction, while it is set to 0 for every other material. The ‘turns’ parameter is set to 1 in every material except for the 4 windings regions, where it is set to 0 because they have been designed with a current density to replace the current circuit and number of turns properties.

Next “mi\_clearselected” is necessary to clear the selection and proceed to define the following object. It is important to assign to each confined area one and only one label otherwise the problem would result as under or over-defined.

At this point, the last region without a label is the circular crown located between windings and PMs meant to be the air gap. This area is assigned with the ‘<No Mesh>’ label, to be skipped during the meshing procedure. Therefore, an air gap property must be added by selecting the circumferences with “mi\_selectarcsegment” and using “mi\_setarcsegmentprop” with the input ‘periodic air gap’ as ‘propane’ and all the others set to 0. The function “mi\_addboundprop” defines the property ‘periodic air gap’. This is required to impose different angular positions on the rotor, to see the behavior of the motor throughout the angle span.

A series of circular shells that emulate the impedance of an unbounded domain is generated with “mi\_makeABC”, where using the Dirichlet boundary conditions will improve the electromagnetics behavior of the motor during the analysis.

Now that geometry and properties are defined, “mi\_probdef” is used to set the frequency to 0, ‘millimeters’ as units, ‘planar’ as type, the depth to D, and the remaining parameters to default values.

## Chapter 3

# Post processor analysis

This chapter deals with the calculation of torque developed by the motor and most importantly how the modifications on the dimensions affect the performance.

The blocks associated with the rotor, that are the core and the two PMs, are selected with “mo\_selectblock” and “mo\_blockintegral” computes the torque on the selected area.

For simplicity the following simulations are performed using the same parameters used by Nasiri-Zarandi, Mirsalim, and Cavagnino in [5]. The only exception is the depth, which is set to 1000 mm to ease the analysis of the results, normalizing the results with respect to the axial length. The dimension applied to the model are:

- $R_{so} = 43.8$  mm
- $R_{si} = 31.25$  mm
- $R_{ri} = 7.5$  mm
- $MC = 1.14$  mm
- $H = 0$  mm
- $\theta_R = 120^\circ$
- $G = 3.56$  mm
- $LM = 4.85$  mm
- $D = 1000$  mm

Several simulations are conducted letting some of the critical parameters increase or decrease in order to see the effect on the torque characteristic curve. For this analysis, the use of “mi\_modifyboundprop” is required to change the orientation

of the rotor. A for-cycle is implemented employing a vector of angles ranging from  $-60^\circ$  to  $60^\circ$  in combination with the function above.

## 3.1 Modifications on the dimensions of the magnets

### 3.1.1 Rotor pole angle arc

The first study is performed by modifying the rotor pole angle arc, that is the angle associated with the permanent magnet's arc. The rotor pole arc affects the

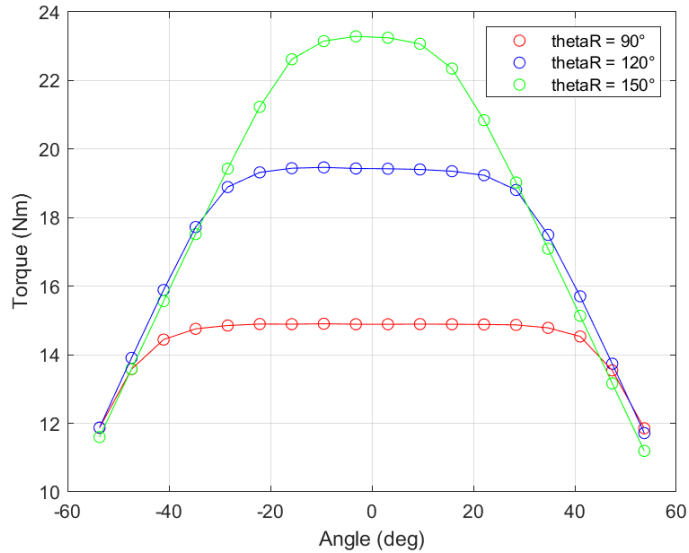


**Figure 3.1:** Torque-angle characteristic curve with different rotor pole angle arcs

dimensions of the PMs so an increase in its dimensions is supposed to produce a bigger magnetic flux resulting in a greater torque. When  $\theta_{R}$  is  $90^\circ$ , the peak torque is 14.9 Nm while when it is  $150^\circ$ , the torque grows to 23.3 Nm, that, compared to the 19.4 Nm obtained with the default dimensions, are respectively 23% lower and 20% greater. The main drawback of this increase in both dimension and output is that the torque characteristic curve assumes a steep shape. It can be seen in figure 3.1 that with the pole arc equal to  $150^\circ$  the torque at the outer limits is 20% lower compared to the peak value, while with the arc equal to  $90^\circ$ , it decreases by less than 1%. As it was expected, the curve is symmetric with respect to the vertical axis, because of the geometric symmetry of the motor.

### 3.1.2 Width of the magnets

A further simulation is performed with a focus on the width of the magnets, whose values is ranging between 4 mm and 5.7 mm. The consequence of this variation is comparable to the previous one but with a significantly lower impact. The effect on the torque is slightly noticeable, as the lower value is 18.2 Nm which is 6% less than the default value, as opposed to the 5% increase recorded on the upper value of 20.3 Nm. Figure 3.2 illustrate how the steepness is minimally affected by the

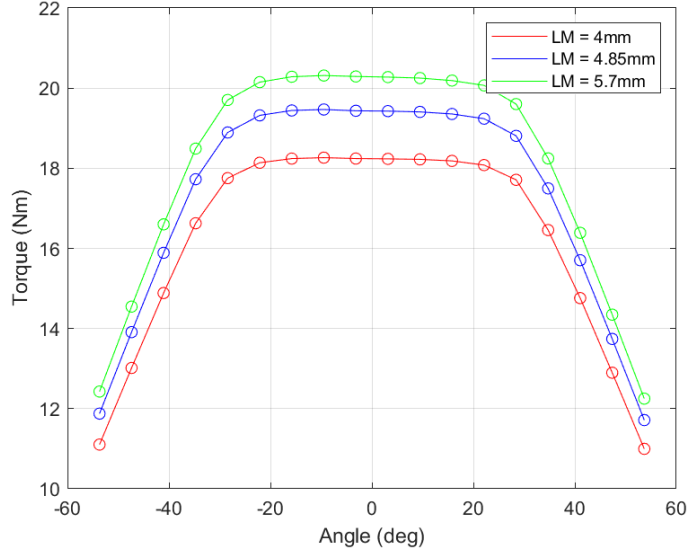


**Figure 3.2:** Torque-angle characteristic curve with different magnet widths

variations of  $LM$ , as the decrease in torque on the outer limits of motion reaches 4% with the thinner PMs and 5% with the thicker ones.

## 3.2 Modifications on the dimensions of the armature windings

### 3.2.1 Air gap (distance between the stator core and PMs)

The third analysis focuses on  $G$  which spans from 2.66 mm to 4.46 mm. Recalling that this parameter directly affects the thickness of the windings ( $WT = G - MC$ ), and also that the block properties defining the windings specified the current density rather than the total current, it is expected to observe an increase in the stator excitation flux proportional to the parameter, meaning an increase in the torque. The lowest  $G$  produces 13.7 Nm, which is 29% lower than the default results, on the

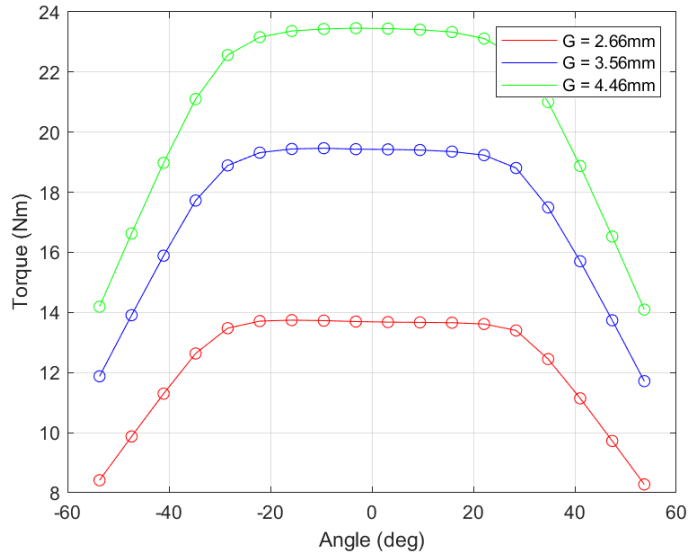


**Figure 3.3:** Torque-angle characteristic curve with different air gaps

other hand, the maximum air gap results in a 21% increase in torque, with a value of 23.5 Nm. The shape of the characteristic curve shown in figure 3.3 is slightly affected as the performance on the limits of motion of the rotor is respectively 4% and 6% lower for smaller and bigger dimensions.

### 3.2.2 Mechanical clearance

An additional simulation deals with the mechanical clearance whose limits are 0.58 mm and 1.70 mm. For the same reason of the previous analysis, this parameter influences the windings thickness, a bigger clearance leaves less space for the windings and increases the magnetic flux barrier effect of the air, thus resulting in a smaller torque. The smallest  $MC$  produces 23.8 Nm, which is 23% greater than the standard, as opposed to the 15.2 Nm obtained with the maximum  $MC$ , which decreases the performance by 22%. It can be observed in figure 3.4 that the rotor position minimally affects the characteristic curve that can be considered flat in both cases, as they both register a 5% drop at 30° from the middle position.

### 3.2.3 Parameter H

The final test is led increasing the value of parameter  $H$  since it is strictly necessary to have a space between upper and lower windings for building reasons. Three simulations are performed with different values of  $H$ : 1 mm, 5 mm, and 10 mm. It can be seen in figure 3.5 that the introduction of this parameter has no effects on

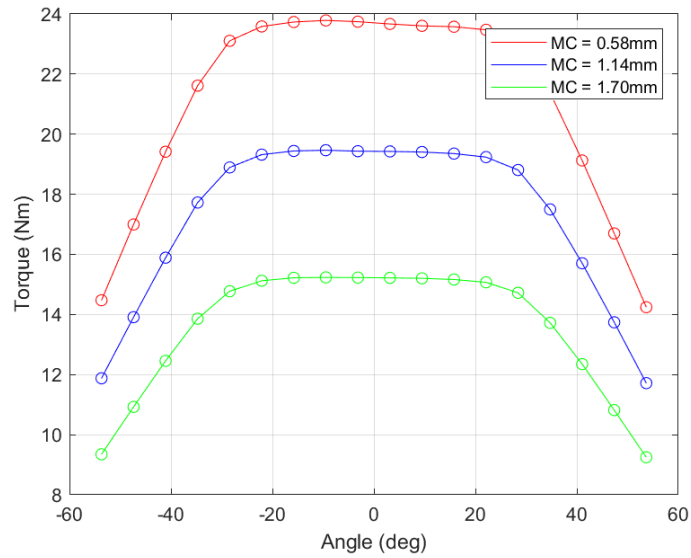


**Figure 3.4:** Torque-angle characteristic curve with different mechanical clearances

the peak torque, as it decreased from the standard by less than 1% in all the cases. An increase of  $H$  reduces the area covered by the windings on both ends, so the effect of a change in this parameter can be noticed only when the rotor position is close to the limits, as the performances decrease respectively by 5%, 9%, and 17% for  $H=1$  mm,  $H=5$  mm, and  $H=10$  mm. This reduction in the area covered by the windings makes the curve steeper.

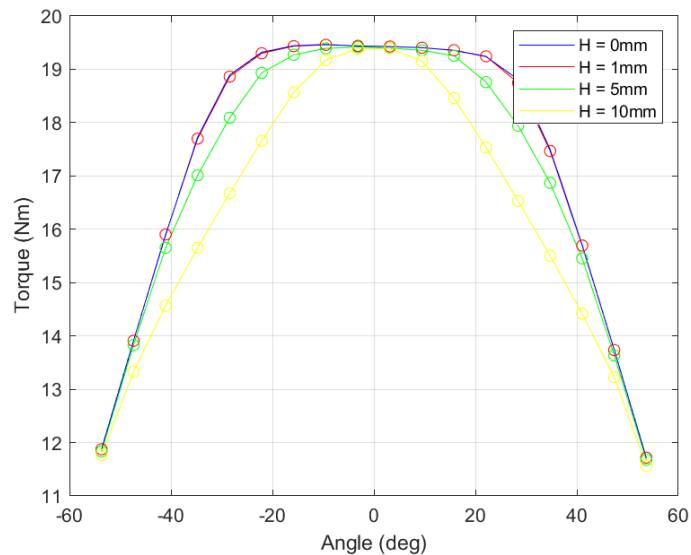


**Figure 3.5:** Torque-angle characteristic curve with different values of  $H$

### 3.3 Considerations on the simulations

The torque in an electric motor is directly proportional to the external product between flux linkage and current. Considering that the magnets are mounted on the surface and that their magnetic permeability is approximately the same as air, the reluctance computed along any direction is constant, so the rotor is isotropic. Recalling the theory on torque production of e-motors, the torque component due to the reluctance is null for isotropic motors. For this reason, the flux linkage only has the PMs component. This flux tends to align the rotor with the magneto-motive force (MMF) generated by the stator, thus producing torque. The first and second analysis deal with the permanent magnet's dimensions, which are directly related to the strength of its magnetic field. As a matter of fact, greater magnets result in greater torque at the expense of an uneven output capacity throughout the whole movement range. The following three simulations focused on the windings dimensions. A bigger windings area allows more current to flow through the wire coils, which produces a greater MMF resulting in increased torque. This relation is true until the current is increased to a critical point at which the ferromagnetic cores become saturated.

Figure 3.6 [13] represents an average ferromagnetic material characteristic that reflects the nonlinear property of the permeability. Two relative permeabilities are associated with the B-H curve. The normalized slope of the B-H curve at any

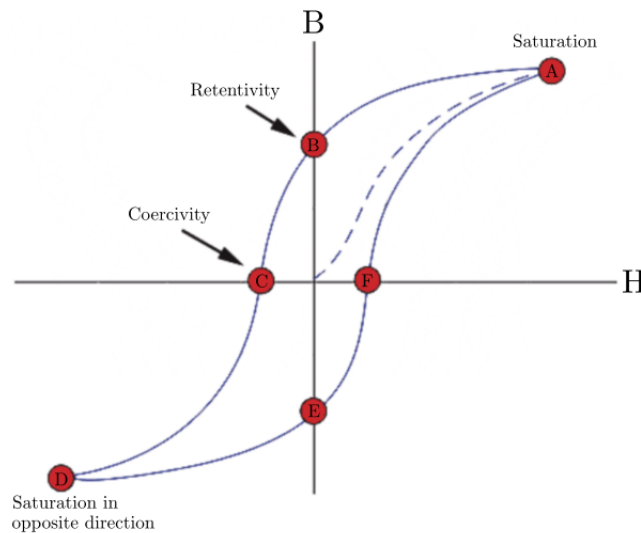


**Figure 3.6:** Hysteresis loop of a ferromagnetic material

point is called the relative differential permeability while the relative amplitude permeability is simply the ratio of  $B$  to  $H$  at a point on the curve and they are given by:

$$\mu_d = \frac{1}{\mu_0} \frac{dB}{dH} \quad (3.1)$$

$$\mu_a = \frac{1}{\mu_0} \frac{B}{H} \quad (3.2)$$

They both are useful to understand the actual condition of the material. Looking at the dotted line, which is the curve representing the unmagnetized material, it can be noticed how the relative amplitude permeability is small for very low excitation, rapidly increases and peaks at medium excitation, and finally decreases for high excitation. On the other hand, the relative differential permeability at very high excitation converges to 1, and the material is said to be in hard saturation. For common electrical steels, hard saturation is reached at a flux density between 1.7 and 2.3 T, and the onset of saturation occurs in the neighborhood of 1.0 to 1.5 T. To avoid core saturation, the maximum flux density of the cores should not exceed the flux density at the knee point of the BH curve.

Saturation can negatively impact the performance of the motor by reducing the amount of torque and power that can be generated and increasing iron losses in the cores and copper losses in the stator windings. When ferromagnetic materials are excited with any time-varying excitation, energy is dissipated due to hysteresis and eddy current losses.

### 3.3.1 Hysteresis losses

Hysteresis loss is caused by the magnetization and demagnetization of the core as current flows in the forward and reverse directions. As represented in figure 3.6 by the outer loop, when the magnetizing force or field intensity  $H$  increases, the magnetic flux density  $B$  does the same. At point "A", the material is said to be saturated and a further increase in the magnetizing force would result in a very little increase in flux.

Then when the field is decreased, the flux does likewise but its decreasing rate is lower. Therefore, when the magnetizing force reaches zero at point "B", the flux density retains a value bigger than zero, the retentivity.

A field in the negative direction must be applied for the flux density to reach zero at point "C", this magnetizing force is called coercivity. Then the field can be decreased until the flux saturates in the opposite direction at point "D".

Completing a full cycle of magnetizing and de-magnetizing and mapping it into a B-H graph draws a hysteresis loop and the area contained by the loop represents the energy lost in the process. Generally, the hysteresis power loss is described by

the following equation:

$$P_h = k_h \cdot f \cdot B_m^n \quad (3.3)$$

Where  $k_h$  is a constant that depends on the material type and dimensions,  $f$  is the frequency of applied excitation,  $B_m$  is the maximum flux density within the material, and  $n$  is a material-dependent exponent between 1.5 and 2.5.

### 3.3.2 Eddy current losses

Eddy current losses are the result of the law of induction formulated by Faraday, who stated that “any change in the magnetic flux surrounding a coil, gives rise to an induced voltage, or electromotive force (EMF), in the same coil, regardless of the causes of the initial change”. Thus, when a ferromagnetic core is rotated in a magnetic field, an EMF is induced in the coils. This induced EMF in turn causes the flow of circulating currents, known as eddy currents, that results in a power loss.

The main strategy to reduce these losses is to build laminated cores, that are made of different thin sheets of metal that are then coated with an insulating material to prevent the induced currents to jump from one sheet to another, like in a short circuit. The resistivity of the material dramatically increases by stacking these laminations together. Considering that the insulating coating is made of a nonconductive and nonmagnetic material, the laminations work also as flux barriers, like for synchronous reluctance motors. Thus, it is important to orient the laminations parallelly to the desired flux direction. A good approximation of the losses due to eddy current is described by the relationship:

$$P_e = k_e \cdot f^2 \cdot B_m^2 \quad (3.4)$$

where  $k_e$  is a constant. In this case, the power lost is proportional to the square of both frequency and maximum flux density. Therefore, hysteresis loss is expected to dominate at low frequencies, and eddy current loss to dominate at higher frequencies. Since both kinds of losses are difficult to isolate experimentally, they together are usually referred to as core losses.

## 3.4 Flux analysis

For the reasons presented above, a flux level tolerance must be set in the two ferromagnetic cores for the following simulations. Considering that the flux in the rotor is generated by the PMs that are in-built on the core, the flux is integral to the core, so the rotational speed of the rotor and flux is the same. This means

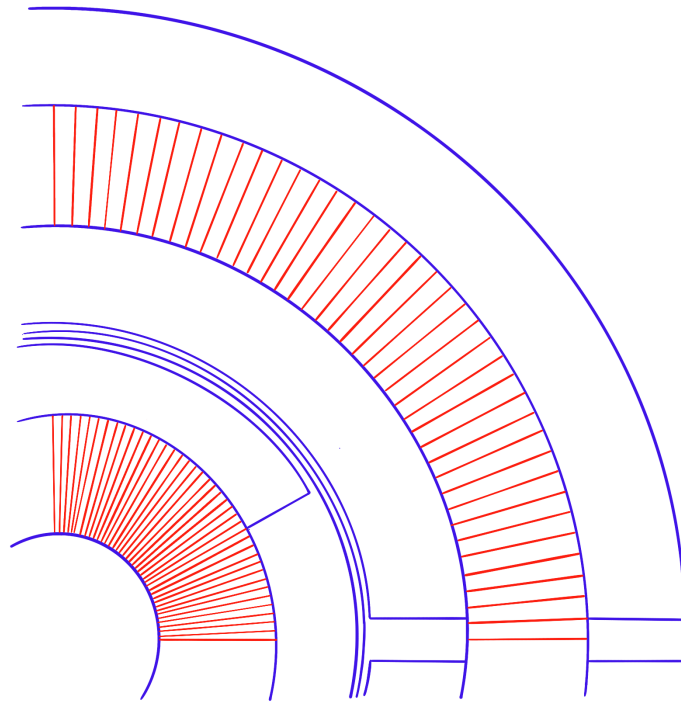


**Figure 3.7:** Radial lines to estimate flux on the cores

that by taking a certain point in the rotor core and computing its flux density during normal operating conditions, the results show how the flux can be considered non-varying. On the other hand, if the same procedure is followed on the stator core, a certain point will record a time-varying excitation with a certain frequency. Recalling that core losses are directly dependent on the frequency of excitation, they are low in the rotor, while they are much more evident in the stator core. For this reason, a tolerance level of 1.4 T is imposed on the rotor core, while in the stator it is set to 1.2 T.

The flux analysis is performed using "mo\_seteditmode" with 'contour' as input and "mo\_addcontour" with the coordinates of a point to specify the two ends of the segment upon which the flux is computed. The function "mo\_lineintegral" gives as a result the total and average flux computed on the specified contour. Several segments radially oriented are drawn on both stator and rotor like shown in figure 3.7, the length of these segments must be equal to the width of the cores. Only the

value corresponding to the average flux is taken into consideration and the greatest one among all the computed ones is appointed as peak flux.

The peak flux of both stator and rotor are then compared to their respective tolerance limits. If at least one of the two peak flux values exceeds his threshold, the geometry is considered invalid and the trial is discarded. Conversely, in case both peak fluxes stay within their limits, the geometry designed is considered viable, therefore its peak torque is stored together with its geometry parameters.

The next step of this project is to find the best possible geometry, which is the

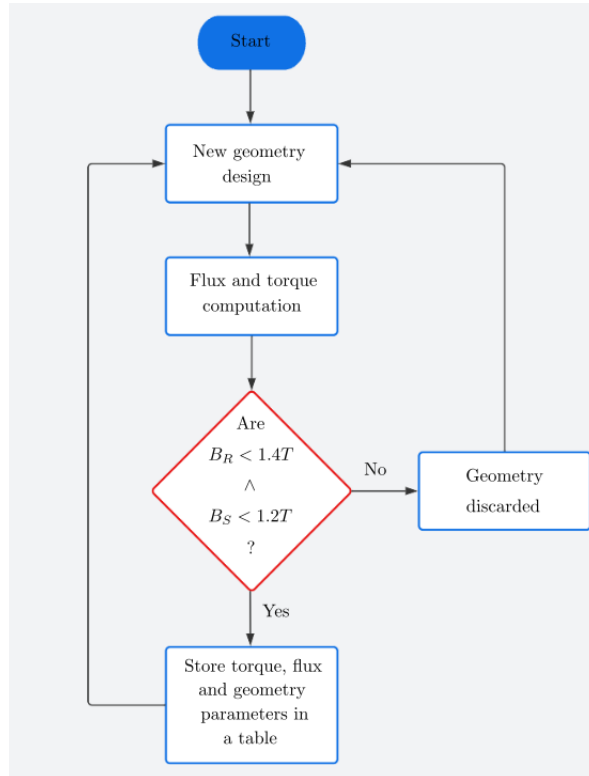


**Figure 3.8:** Flow chart to pick viable geometries

one developing the greatest torque among the motors that satisfy the flux density conditions.

The work done in this chapter has demonstrated the basic relationship between parameters and performances but changing the parameters manually and storing the results for every iteration could result in a tedious and also not efficient process. For this reason, an optimization algorithm is used to speed up the process and find the best solution.

# Chapter 4

## Parameter optimization

Optimization algorithms are a set of mathematical methods used to find the best or optimal solution to a problem, typically involving maximizing or minimizing an objective function.

### 4.1 Choice of the optimization algorithm

They can be sorted into two categories: deterministic and stochastic algorithms. A deterministic optimization algorithm is designed to find the optimal solution to a problem based on a set of fixed rules and parameters. It follows a predefined set of steps to reach a specific solution, typically the best possible one based on the given inputs and constraints.

On the other hand, stochastic optimization algorithms have a randomness factor in the optimization process. These algorithms are designed to find a good solution to a problem by exploring the search space for possible solutions in a probabilistic manner. Instead of finding the best solution, stochastic optimization algorithms aim to find a good solution that satisfies the given constraints with a high probability. Deterministic algorithms are typically faster and more precise, but they may not be suitable for complex problems with a large search space. Stochastic algorithms are more versatile and can handle complex problems with a large search space, but they may require more time to converge to a good solution. Sidorov, Semenkin, and Minker presented in [14] a classification of different algorithms shown in 4.1. Due to the presence of a random factor, a stochastic algorithm is much less likely to solve different problems following the same solution path, in comparison with deterministic algorithms, which, given the same input and initial condition, will always give the same result, following a precise sequence of actions. That is the reason why a stochastic algorithm is chosen to carry on the work.

Heuristic optimization algorithms are problem-specific techniques that use rules of

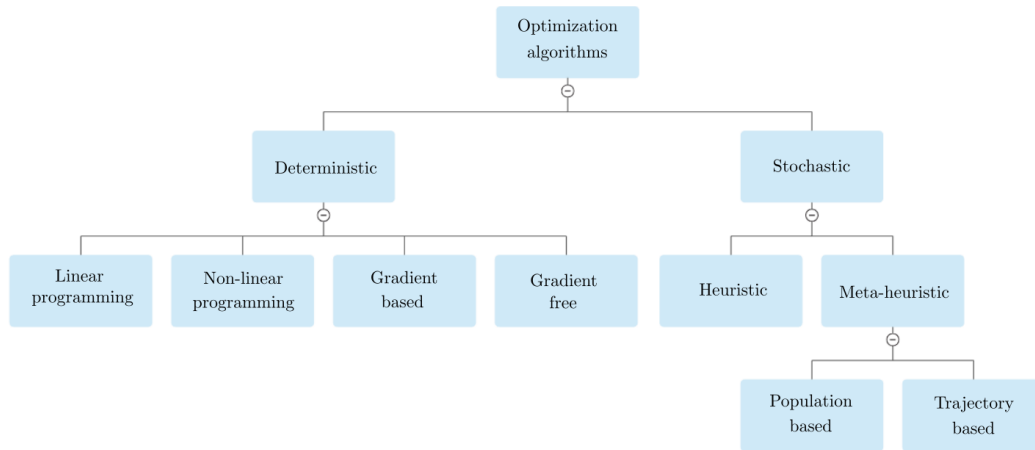


**Figure 4.1:** Classification of optimization algorithms

thumb or domain knowledge to guide the search for solutions. They are generally designed to solve specific types of problems and rely on specific problem structures to guide the search process. On the other hand, meta-heuristic optimization algorithms are general-purpose algorithms that can be applied to a wide range of problems without requiring prior knowledge of the problem structure. They are typically inspired by natural phenomena, such as the behavior of animals, and aim to explore the search space efficiently and effectively. In general, meta-heuristic optimization algorithms are considered more powerful and flexible than heuristic optimization algorithms, as they can be applied to a wide range of problems without requiring prior domain knowledge.

Trajectory-based algorithms use a single agent or solution which moves through the design space or search space in a piece-wise style. The steps trace a trajectory in the search space, with a non-zero probability that this trajectory can reach the global optimum. On the contrary, population-based optimization algorithms maintain a population of candidate solutions and iteratively update them to improve the overall quality of the solutions. These algorithms are typically used for solving optimization problems in which the objective function is non-linear and has many local optima.

### 4.1.1 Population based algorithms

The choice of best parameters is performed by implementing a population-based optimization algorithm. The optimization of the performances of a motor is done by working on multiple variables, thus the objective function is expected to be complex with its search space containing multiple peaks.

The random factor of stochastic algorithms combined with a large number of candidate solutions of population-based algorithms makes this category suitable for the matter in question. Some examples of population-based optimization algorithms described in [15] include:

- Particle Swarm Optimization (PSO): inspired by the communal activities of animals such as bird flocking or fish schooling. The population is called a swarm and every member of the swarm is called a particle representing a candidate solution. Every candidate has a position in the search space, fitness value, and velocity as its associated parameters. All the particles initially assume random positions and then move around communicating good positions to each other. The velocity and position of every member are updated based on the best performance of the particle and the best performance of the swarm. PSO is useful in a wide range of optimization problems but has the drawback of falling into local optimum points while optimizing complex multimodal functions
- Ant Colony Optimization (ACO): inspired by the behavior of ants. It mimics their ability to find the shortest routes from their nest to food. The ants follow a simple set of rules that are based on the natural behavior of real ants. They move through the solution space, depositing pheromones along the way, and following the pheromone trails laid down by other ants. The pheromone trails are used as a form of communication between the ants, and they act as a kind of global memory for the colony. Ants are more likely to follow paths with stronger pheromone trails, so over time, the trails converge toward the optimal solution. It is a robust algorithm but not suitable for large-scale combinatorial or continuous problems
- Artificial Bee Colony (ABC): stimulated by the foraging behavior of honey bee swarms, that search for food and carry back nectar to the hive. The three categories of bees used in ABC are employers, onlookers, and scouts. In the ABC algorithm, the employed bees search for food sources in the search space, while the onlooker bees select food sources based on the information provided by the employed bees. The scout bees randomly search for new food sources if the employed and onlooker bees cannot improve the quality of the population. It is simple, efficient, and easy to implement, however, it is very sensible in the selection of its parameters and slows to converge
- African Buffalo Optimization (ABO): modeled after the herd behavior of African buffalos. These animals are known for their strong social behavior and ability to collectively find food and water sources. ABO mimics this behavior by dividing the population into herds and allowing them to search for the optimal solution independently. Each herd is composed of a leader and several

followers. The leader is responsible for leading the herd towards promising areas of the search space, while the followers explore the surrounding area. The leader is chosen based on its fitness value, and the followers are chosen based on their proximity to the leader. ABO uses a set of update rules to adjust the positions of the buffalos based on their fitness values. The update rules are designed to encourage exploration of the search space and avoid premature convergence to local optima. This algorithm is relatively recent, as it was developed only in 2014

PSO is the chosen algorithm because of its adaptability to a wide range of problems, including function optimization, and its effectiveness with high-dimensional search spaces and non-linear optimization problems. However, his tendency to converge to local optima must be taken into account and solved with careful parameter tuning.

### 4.1.2 Particle swarm optimization

The algorithm uses the concept of a swarm of particles that move in the search space, updating their positions based on their own best performance and the best performance of their peers. The search space, or design space, is the domain of the objective function that the algorithm is trying to optimize. Its dimensions are defined by the number of variables in the objective function. The size and complexity of the design space can have a significant impact on the performance of the algorithm. Large search spaces with many local optima can make the convergence of the algorithm to the global optimum difficult. On the other hand, small search spaces with few constraints ease the search for the optimum.

Each particle represents a potential solution to the problem. The position in the search space corresponds to the values of the parameters of the function being optimized, while the velocities determine how they move in the search space. The algorithm starts with an initial population of particles, each with a randomly assigned position and velocity. As the algorithm progresses, the particles move through the search space, and their velocities and consequently their positions are updated based on the following two factors:

- The particle's personal best position ( $pbest_i$ ): the best position that the particle has encountered so far in the search space. The particle's velocity is updated to move it toward its personal best position
- The global best position ( $gbest$ ): This is the best position that has been encountered by any particle in the swarm. The particle's velocity is also updated to move it toward the global best position

The formulas that determine the position and velocity of each particle are the following:

$$v_i(t + 1) = w \cdot v_i(t) + c_1 \cdot r_1 \cdot (pbest_i - x_i(t)) + c_2 \cdot r_2 \cdot (gbest - x_i(t)) \quad (4.1)$$

$$x_i(t + 1) = x_i(t) + v_i(t + 1) \quad (4.2)$$

where:

- $v_i(t + 1)$  is the updated velocity of particle  $i$
- $w$  is the inertia weight, which controls the influence of the particle's previous velocity
- $c_1$  and  $c_2$  are acceleration coefficients that respectively control the influence of the particle's personal best position and the global best position
- $r_1$  and  $r_2$  are random numbers between 0 and 1
- $x_i(t)$  is the current position of particle  $i$

The movement of the particles continues iteratively, with the velocities and positions of the particles being updated at each iteration. The stopping criteria determine when the algorithm should terminate. There are several common stopping criteria:

- Maximum number of iterations: This is the simplest and most commonly used stopping criterion. The algorithm terminates after a specified number of iterations
- Convergence: The algorithm terminates when the particles have converged to a specific solution or when the improvement in the objective function value is below a specified threshold
- Time limit: The algorithm terminates after a specified amount of time has elapsed
- No improvement: The algorithm terminates when there has been no improvement in the objective function value over a specified number of iterations
- Budget limit: The algorithm terminates when a specified budget, such as the number of function evaluations, has been reached

The choice of stopping criterion depends on the problem being solved and the resources available. A budget limit criterion is used when the objective function is expensive to evaluate. Similarly, if the algorithm is being used in a real-time application, a time limit may be more appropriate than the other criteria. It is

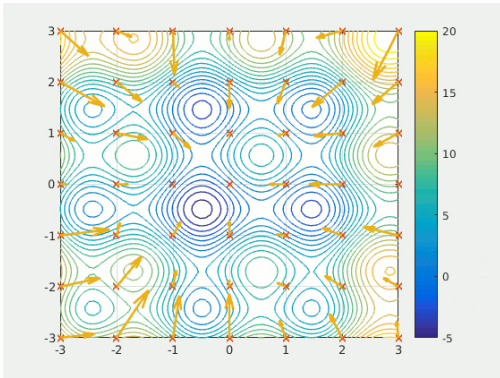


**Figure 4.2:** Initial position of the swarm

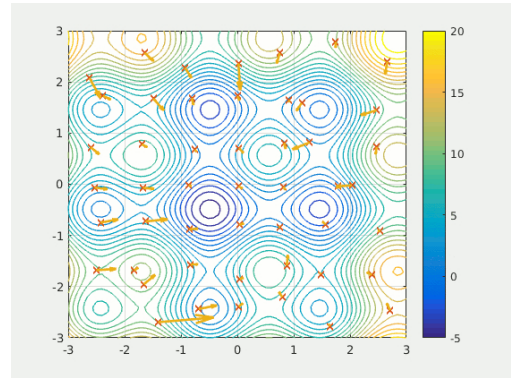


**Figure 4.3:** Position of the swarm after 5 iterations

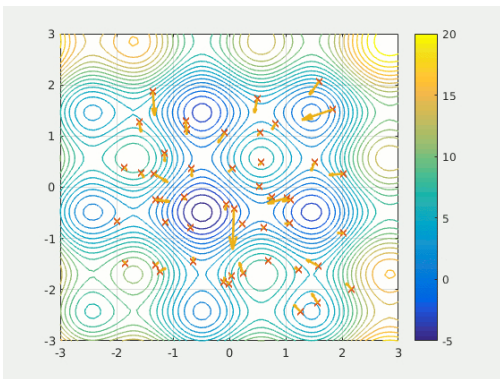


**Figure 4.4:** Position of the swarm after 10 iterations

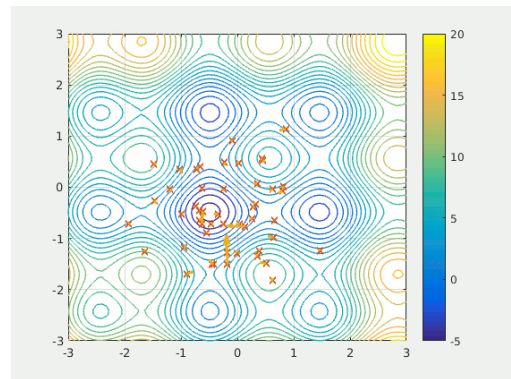


**Figure 4.5:** Position of the swarm after 20 iterations

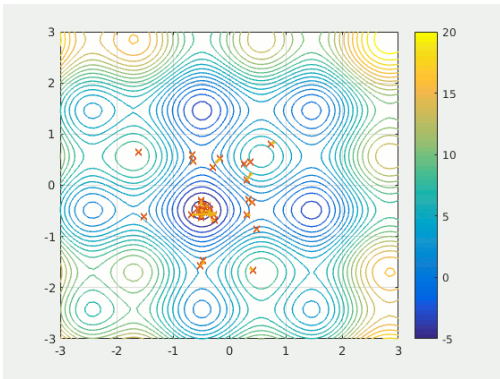


**Figure 4.6:** Position of the swarm after 50 iterations

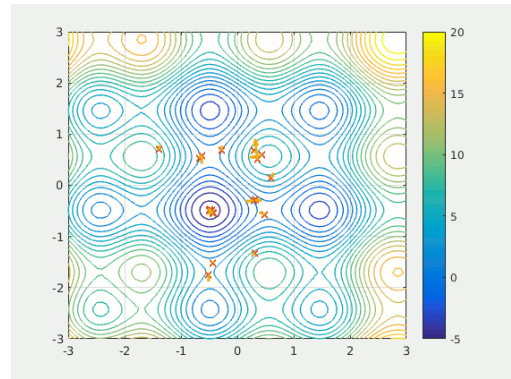


**Figure 4.7:** Position of the swarm after 100 iterations

important to note that choosing an appropriate stopping criterion is critical to the success of the optimization process. A premature termination of the algorithm may result in sub-optimal solutions, while an excessively long run-time can be computationally expensive and impractical.

The images from 4.2 until 4.7 are taken from [16] and they show an example of how the swarm moves as the iterations progress. It can be noticed how the particles initially have a random distribution in a two-dimensional search space. Then the whole swarm tends to move towards those particles that have the best fitness value. The iterations carry on until a stopping criterion is met.

## 4.2 Implementation of the algorithm

The MatLab function "particleswarm(fun, nvars, lb, ub, options)" is employed to perform the optimization. It gives as output a vector that achieves a local minimum of "fun". The dimension of this vector is equal to the value specified by "nvars", which also defines the number of variables or dimensions of the search space. Since the algorithm attempts to find a minimum, the function to be minimized presented in the appendix is the integral of the torque computed on the rotor core and its surface-mounted PMs with a minus sign. Furthermore, "lb" and "ub" determine the lower and upper bounds of the design space, in particular, they are two vectors with dimensions equal to the number of variables. Finally "options" allows to set additional parameters like:

- "FunctionTolerance": iterations end when the relative change in best objective function value over the last "MaxStallIterations" (another option parameter) iterations is less than this value
- "MaxIterations": is the maximum number of iterations the algorithm can take
- "MaxStallTime" and "MaxTime": respectively the maximum number of seconds without an improvement in the objective function and the maximum time that the algorithm can run
- "SwarmSize": number of particles in the swarm, also meaning the number of simulations performed at the same time

The search space chosen is tridimensional and the three variables of matter are air gap ( $G$ ), permanent magnet thickness ( $LM$ ), and stator inner radius ( $R_{si}$ ). The stopping criterion employed in the project is the tolerance and it is set to  $10^{-3}$ . The maximum number of stall iterations is not specified, so it assumes its default value of 20. The option display is used in combination with 'iter' to show on the command line of MatLab the result of every iteration of the algorithm.

Swarm size	LB (mm)	UB (mm)	Optimum result (mm)	Torque (Nm)	Max rotor flux (T)	Max stator flux (T)
10	1.5;1.5;15	4.5;4.5;25	4.50;3.47;19.61	7.2377	1.3714	1.1999
20	1.5;1.5;15	4.5;4.5;25	4.50;3.49;19.59	7.2643	1.3798	1.199
30	1.5;1.5;15	4.5;4.5;25	4.50;3.41;19.43	7.0306	1.3703	1.1476
10	1.5;1.5;15	5;5;25	4.99;3.18;19.59	7.1984	1.284	1.1484
10	1.5;1.5;15	5;5;25	4.99;3.36;19.37	7.1668	1.3782	1.1179
10	1.5;1.5;15	5.5;5;25	5.49;3.26;19.44	7.2563	1.3596	1.1194
10	1.5;1.5;15	5.7;4.5;25	5.69;3.25;19.43	7.2761	1.3707	1.1191
10	1.5;1.5;15	5.8;4.5;25	5.57;3.27;19.43	7.2822	1.369	1.1193
20	1.5;1.5;15	5.8;4.5;25	5.65;3.25;19.43	7.3016	1.3687	1.1185
30	1.5;1.5;15	5.75;4;25	5.63;3.26;19.43	7.3073	1.369	1.1188
30	1.5;1.5;15	5.75;4;25	5.75;3.24;19.44	7.2865	1.3719	1.1196
10	1.5;1.5;15	5.75;4;25	5.65;3.26;19.43	7.2942	1.3719	1.1193
10	1.5;1.5;15	5.75;4;25	5.75;3.26;19.42	7.2968	1.3797	1.1178
10	1.5;1.5;15	5.85;4;25	5.24;2.93;19.64	7.013	1.1966	1.1195
10	1.5;1.5;15	5.85;4;25	5.77;3.19;19.46	7.2469	1.3469	1.1198
10	1.5;1.5;15	5.85;4;25	5.59;3.15;19.78	7.5059	1.2764	1.1997
30	1.5;1.5;15	5.85;4;25	5.85;3.22;19.71	7.5119	1.3284	1.1975
30	1.5;1.5;15	5.85;4;25	5.63;3.39;19.64	7.6214	1.3905	1.1982
20	1.5;1.5;15	5.85;4;25	5.74;3.39;19.64	7.6579	1.401	1.1986
20	1.5;1.5;15	5.85;4;25	5.62;3.40;19.64	7.6499	1.3937	1.1997
20	4;2.5;18	6;4;22	5.63;3.41;19.64	7.667	1.4	1.1993
30	4;2.5;18	6;4;22	5.77;3.34;19.66	7.6382	1.3803	1.1998
30	4;2.5;18	6;4;22	5.05;3.50;19.62	7.5276	1.401	1.1998
30	4;2.5;18	6;4;22	5.75;3.38;19.63	7.6219	1.3985	1.1964
10	4;2.5;18	6;4;22	5.60;3.41;19.64	7.6491	1.398	1.1983
10	4;2.5;18	6;4;22	5.48;3.42;19.63	7.604	1.3922	1.1945
10	4;2.5;18	6;4;22	5.51;3.45;19.63	7.638	1.3952	1.1933
20	4;2.5;18	6;4;22	5.37;3.42;19.65	7.614	1.3945	1.1948
20	4;2.5;18	6;4;22	5.36;3.50;19.64	7.577	1.3976	1.1932
20	4;2.5;18	6;4;22	5.42;3.51;19.63	7.493	1.3934	1.1978
20	4;2.5;18	6;4;22	5.39;3.37;19.66	7.581	1.3955	1.1945
20	4;2.5;18	6;4;22	5.40;3.53;19.60	7.487	1.3935	1.1933
20	4;2.5;18	6;4;22	5.46;3.67;19.48	7.513	1.3964	1.1948

**Table 4.1:** Results of several optimization runs

Lastly, the only parameters left to set are swarm size and lower and upper bounds, which will be tuned after each iteration to achieve the best result possible. The dimension of the swarm size is crucial and must be set accurately so that the particles are enough to quickly converge to the optimum and not too many to make the algorithm slow and heavy. On the other hand, the bounds are critical too because, setting one of the ranges too wide could generate an inconsistent and unfeasible geometry, resulting in an error and consequently in a premature stop of the algorithm, without producing any result. It must be specified that the depth of the motor is set to 1000 mm to normalize the torque with the length, thus interpreting the results easily.

The results presented in table 4.1 show only the simulations that managed to find a local minimum for the objective function. Analyzing the data, it can be noticed how the bounds have been progressively modified to ease the operation. Once it has been assessed that the optimum value of G is around 5 mm, there is no point to leave the lower bound at 1.5 mm, increasing the risk of producing an unfeasible geometry that would result in an error, thus without producing any result. The same reasoning can be applied to the other parameters.

Moreover, some of the simulations produced a geometry able to develop a decent

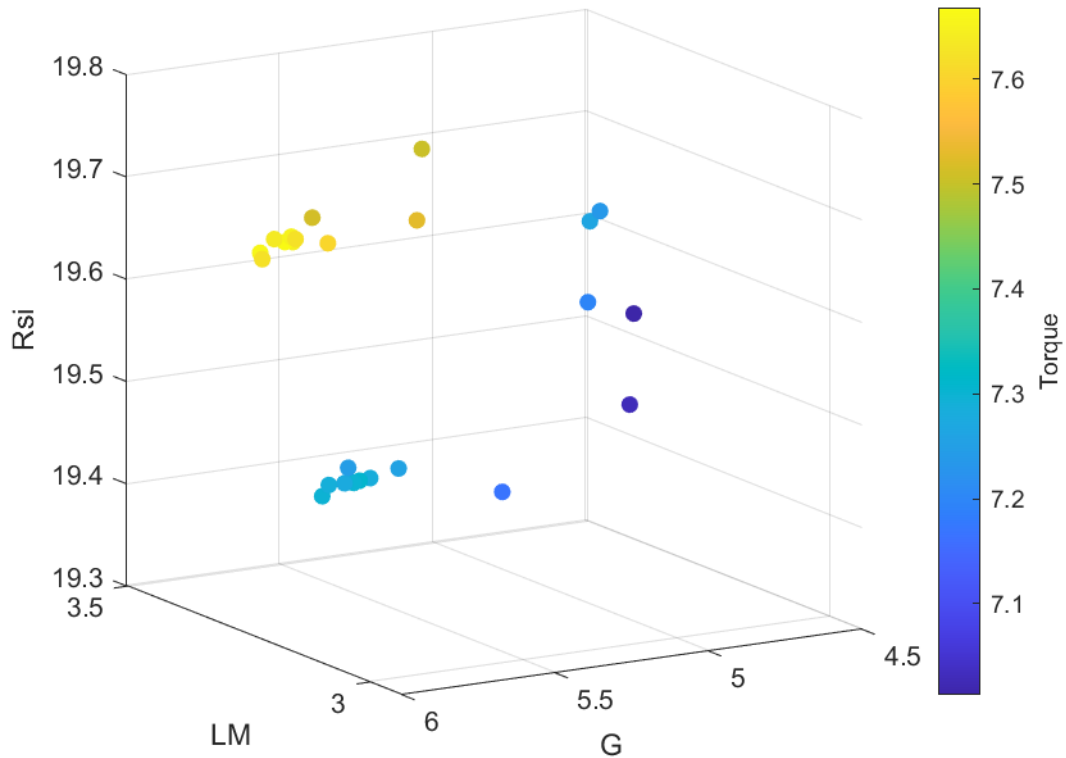


Figure 4.8: 3D distribution of the results of PSO

value of torque, while having the peak flux in either rotor or stator not as close to the limits as it could have been. This is a sign of under-usage, that is to say, the algorithm is not exploiting the full potential of the motor.

The opposite problem is solved by applying an "if" condition that associates a null value of torque to geometries exceeding the flux thresholds, so that the particles tend to avoid the area around it, knowing it yields the worst possible result in terms of performance.

Finally, it can be noticed how the function resulted very complex and with many local optimum points in a very restricted region of the search space. Figure 4.8 plots the results of the optimization, where the three-dimensional space is the search space and the color gradient expresses the different values of torque, with its scale on the side.

## Chapter 5

# Results and conclusions

The optimized parameters shown in figure 4.8 tend to converge to three major regions where local minimums are located. One of these areas yields better results than the others. The simulations performed highlighted a specific point in the design space, that corresponds to the following dimensions:

- $G = 5.6mm \pm 0.1mm$
- $LM = 3.4mm \pm 0.1mm$
- $R_{si} = 19.6mm \pm 0.1mm$

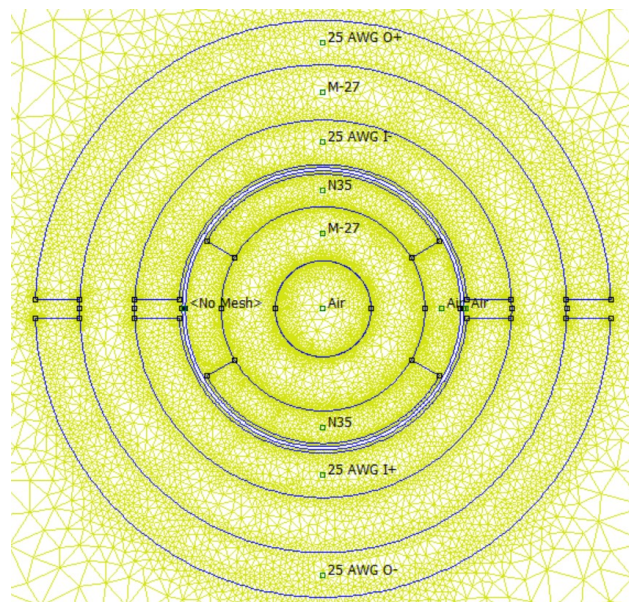


**Figure 5.1:** Final version of the geometry with meshes

The final geometry is shown in figure 5.1, where the yellow triangles are the meshes required by the finite element analysis. Finally, the analysis is run and the command "mi\_loadsolution" is used to generate and view the ".ans" file, marking the limit between pre- and post-processor analysis.

In this other environment, no modifications can be applied to the model, the only tools available allow to compute the quantities of interest, which, in this case, are torque and peak flux in the ferromagnetic cores.

## 5.1 Optimization results

The finite element analysis is implemented in magneto-static mode to evaluate the performances of the optimized design of the limited-angle torque motor. The figures 5.3 and 5.2 show the magnetic flux lines of the motor in case the windings are energized or not. It must be noted that the unbounded domain with the Dirichlet boundary condition was critical to making the effective flux lines so clear and easy to understand.

Furthermore, the distribution of the magnetic flux density with and without current

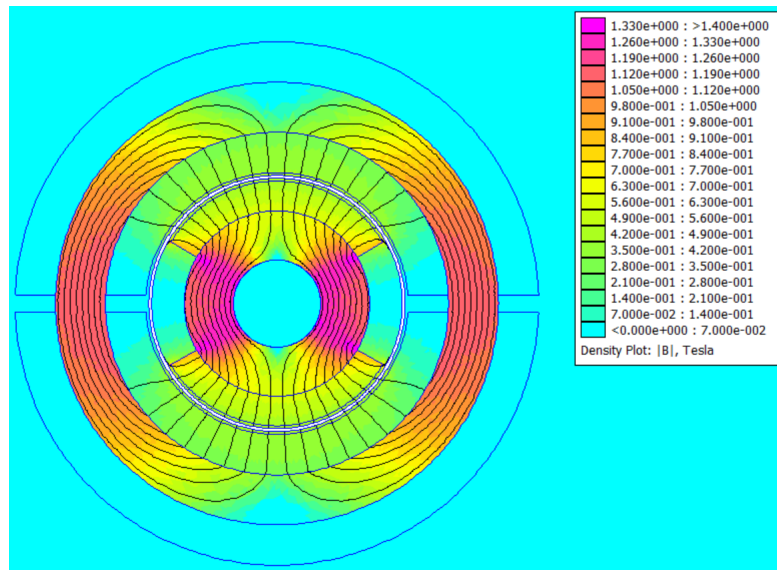
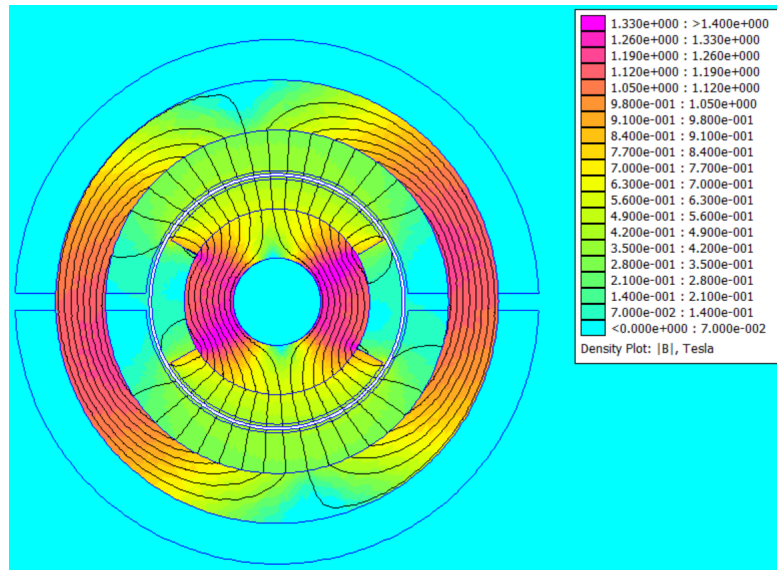


Figure 5.2: FEA of LATM without stator excitation

flowing through the armature windings shows how the flux limitations imposed are perfectly respected. As a matter of fact, the rotor peak flux computed with excited windings is 1.3996T, while in the stator it reaches 1.1996T. It can be noticed how the flux lines without stator excitation are symmetric because the only component in the flux is due to the permanent magnets which are in the middle position.



**Figure 5.3:** FEA of LATM with stator excitation

In the other case, it is easy to notice that the symmetry is lost, highlighting the tendency of the rotor to move when attaining this configuration of position and current, as a result of the interaction between the two fluxes.

Figure 5.4 shows the flux density in the air gap in relation to the angle. The position

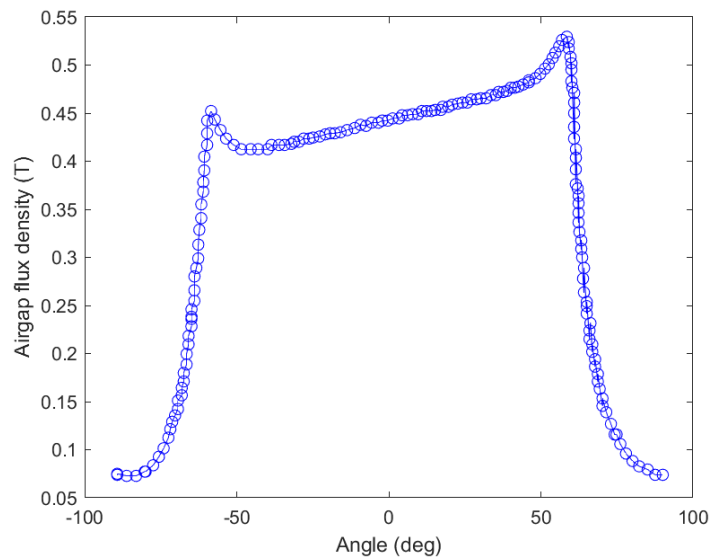


**Figure 5.4:** Air gap flux density over rotor angle

associated with  $0^\circ$  corresponds to the rotor attaining the middle position, symmetric

with respect to the motor geometry. It is easy to notice how in correspondence of  $\pm 90^\circ$  there are the global minima, where the motor develops the lowest torque, these points are outside of the operating area. The figure shows two local maxima around the regions  $\pm 60^\circ$ . These spikes are  $120^\circ$  away from each other, which is exactly the value of  $\theta_R$ , thus this behavior is related to the discontinuities in the geometry.

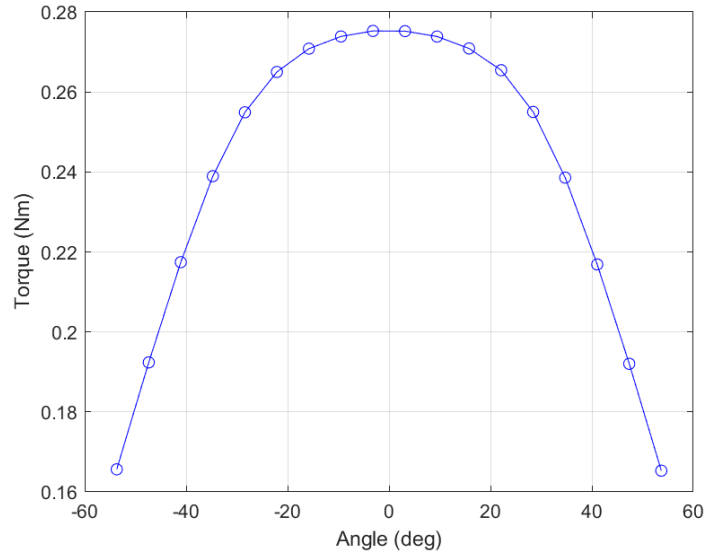


**Figure 5.5:** Torque-angle characteristic

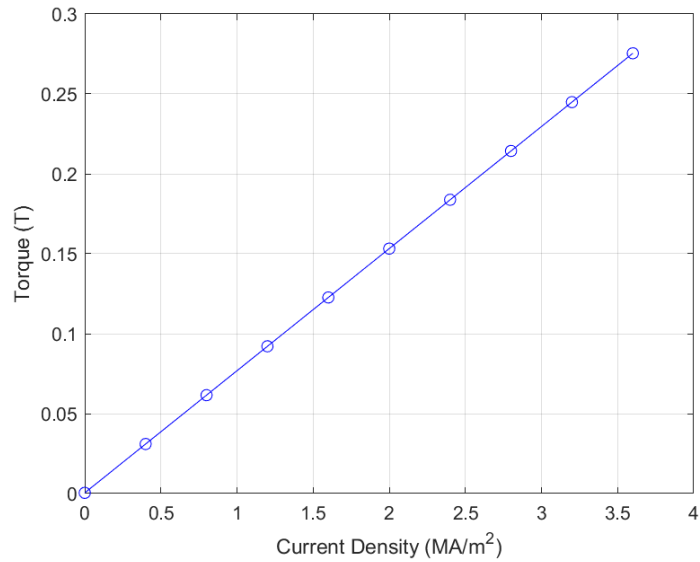


**Figure 5.6:** Torque-current density characteristic

Figure 5.5 shows the relationship between torque developed and pole angle degree. The peak torque is 0.2754Nm, while the torque at the ends of the operating range is 0.251Nm, which is less than 9% lower than the maximum torque. For this reason, the characteristic curve can be considered flat in the working area.

Figure 5.6 presents the ratio between torque and current density. As it was expected, the relationship is linear, as a matter of fact, the two quantities are directly proportional until the saturation of one of the ferromagnetic cores. The constant slope of the curve validated the choice of current density made during the design part.

## 5.2 Comparisons

The torque achievable by the LATM does not match the requirements specified at the beginning of the project, thus it is compared to other motors to get a better understanding of the benefits and drawbacks of the design performed.

### 5.2.1 Increased diameter on the same simulation environment

A further simulation is performed by applying some of the dimensions of [5] to the developed geometry. The parameters used are the same employed in chapter 5 but parameter  $H$  is set to 1mm and the depth to 36mm, so that the results can be compared without further rescaling process. The peak torque of the increased

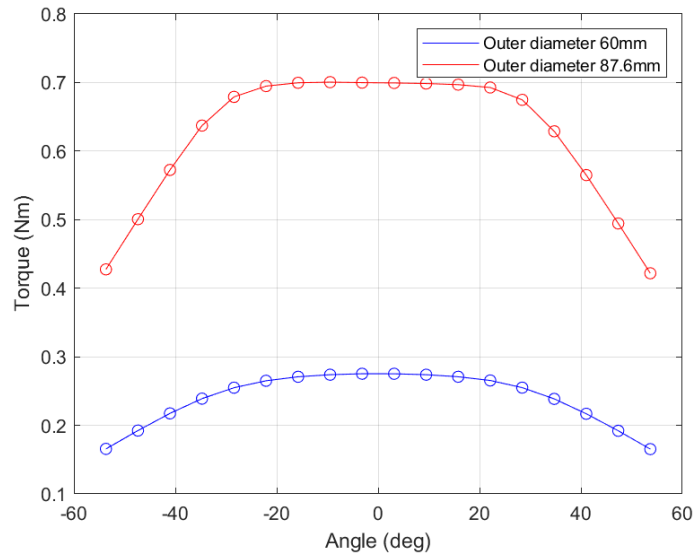
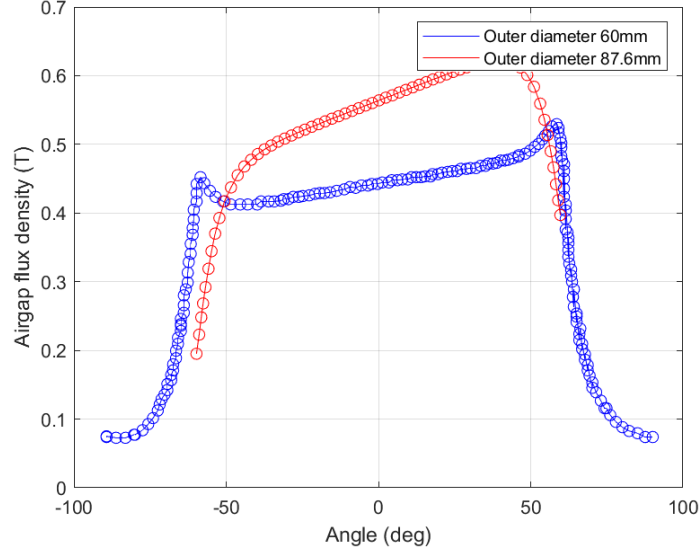


Figure 5.7: Torque-angle characteristic comparison



**Figure 5.8:** Air gap flux density of the two simulated geometries

geometry is  $0.7005\text{Nm}$ , which is 154% greater than the peak torque of the geometry designed, this is due to the 46% increase in diameter. As a matter of fact, the relation between torque and dimensions is often stated as:

$$T = k \cdot R^2 \cdot D \quad (5.1)$$

where  $k$  is a constant,  $R$  is the radius and  $D$  is the axial length.

It can be argued that the torque is directly proportional to the volume of the motor. The volume of the LATM designed,  $V_D$ , and the volume of the new LATM with increased diameter,  $V_N$ , is computed as:

$$V_D = \pi \cdot R_{so}^2 \cdot D = \pi \cdot (25.3751\text{mm})^2 \cdot 36\text{mm} = 72823\text{mm}^3 = 7.2823 \cdot 10^{-5}\text{m}^3 \quad (5.2)$$

$$V_N = \pi \cdot R_{so}^2 \cdot D = \pi \cdot (43.8\text{mm})^2 \cdot 36\text{mm} = 216970\text{mm}^3 = 2.1697 \cdot 10^{-4}\text{m}^3 \quad (5.3)$$

The further step is the computation of the torque density of each geometry:

$$\frac{T_D}{V_D} = \frac{0.2754\text{Nm}}{7.2823 \cdot 10^{-5}\text{m}^3} = 3781.8 \frac{\text{Nm}}{\text{m}^3} \quad (5.4)$$

$$\frac{T_N}{V_N} = \frac{0.7005\text{Nm}}{2.1697 \cdot 10^{-4}\text{m}^3} = 3228.6 \frac{\text{Nm}}{\text{m}^3} \quad (5.5)$$

Considering that the simulations are performed using the same material properties, same current density, same axial length, and same parameter  $H$ , which produces

an even smaller effect due to the bigger dimensions of the new LATM, the torque generated can't be equal to the one reported on the paper. As a matter of fact, the calculations confirm how the smaller geometry reached a global optimum in the design phase, while the motor with increased dimensions has a lower torque density because it did not go through an optimization process.

Looking more in detail at figure 5.7, it can be noticed how they both can be considered flat in the interval spanning from  $-30^\circ$  to  $+30^\circ$ . While focusing on figure 5.8, the geometry with increased diameter has a better air gap performance. As a matter of fact, a greater flux density in the air gap is directly related to the greater torque output of this new simulated motor.

### 5.2.2 LATM from paper [5]

A further comparison is done with the characteristics of the motor taken directly from the paper without intermediate steps or simulations. The motor can produce

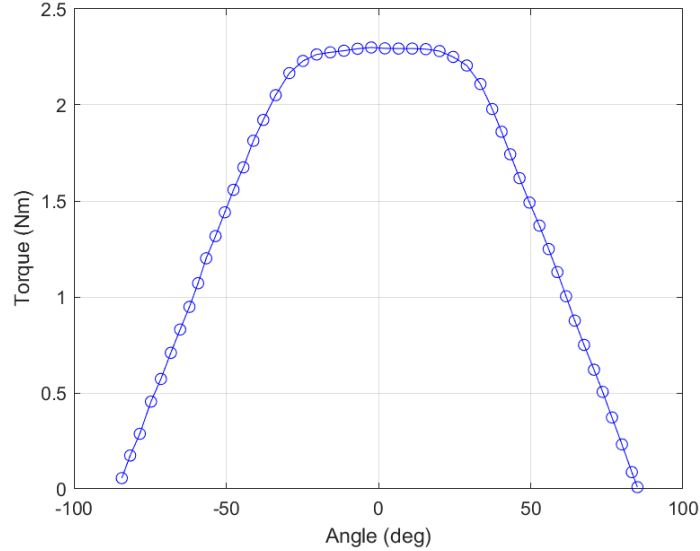


**Figure 5.9:** Torque-angle characteristic curve taken from [5]

2.2994 Nm as peak torque,  $T_P$ , which is considerably greater than the simulations. The behavior is again linear in the range  $\pm 30^\circ$ , then it steeply decreases towards both ends.

Considering that its axial length is 50mm, its volume  $V_P$  and subsequently its torque density are computed.

$$V_P = \pi \cdot R_{so}^2 \cdot D = \pi \cdot (43.8mm)^2 \cdot 50mm = 301350mm^3 = 3.0135 \cdot 10^{-4}m^3 \quad (5.6)$$

$$\frac{T_P}{V_P} = \frac{2.2994Nm}{3.0135 \cdot 10^{-4}m^3} = 7630.3 \frac{Nm}{m^3} \quad (5.7)$$

The LATM presented in the paper has a substantially greater torque density. Its torque is scaled according to the ratio between the two different axial lengths and compared to the previous results, in order to give a better understanding of this result. The curves from figure 5.10 show how the geometry presented in the

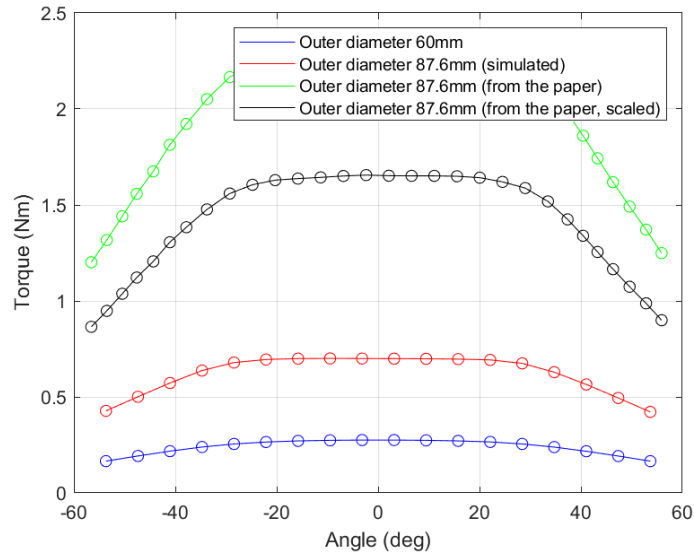


**Figure 5.10:** Torque-angle characteristic with scaled torque

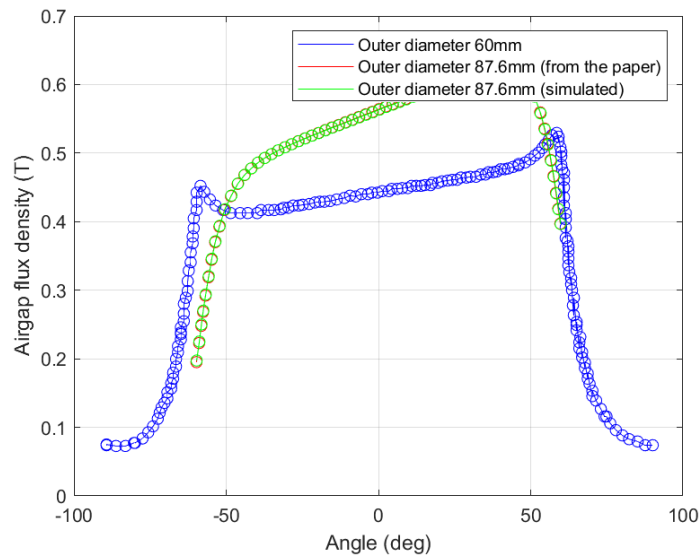


**Figure 5.11:** Airgap flux density of different geometries simulated and the one taken from the paper

paper can produce a much greater torque maintaining the same operative range. The comparison with the torque developed by the simulated geometries has to be carefully used because of the different materials employed, which have distinct magnetic properties, evidently producing contrasting results.

Figure 5.11 presents the air gap flux densities of different geometries. In this case, there is no need to rescale the results with respect to the length of the motor since it does not influence the performance at the air gap. Whichever the length, the flux density between the stator and rotor depends obviously on the fluxes linked, thus on the materials employed for the cores and the magnets and the current applied to the armature, but mostly on the dimension of the air gap itself, namely the geometry of the section. It can be noticed how the flux density of the increased geometry simulated is substantially equal to the one taken from the paper, as a matter of fact, the green line is substantially superimposed to the red line.

### 5.2.3 3-Phase motor

The last comparison is made with a 3-phase motor designed by Prof. Galluzzi [17]. It has the same size as the motor designed in this paper, with the outer diameter equal to 60mm and axial length equal to 36mm. The stator is slotted and houses the distributed 10-pole windings. The rotor has 10 permanent magnets mounted on its surface. Figure 5.12 shows the section of this motor. In the stator, each of the three colors indicates a phase of the windings, while in the rotor it can be observed how there are only two colors, each stating a polarization of the magnet.

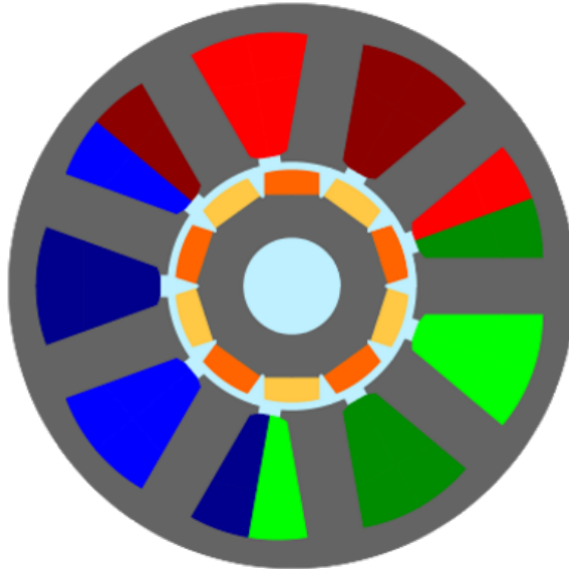


**Figure 5.12:** 3-Phase motor structure taken from the design report

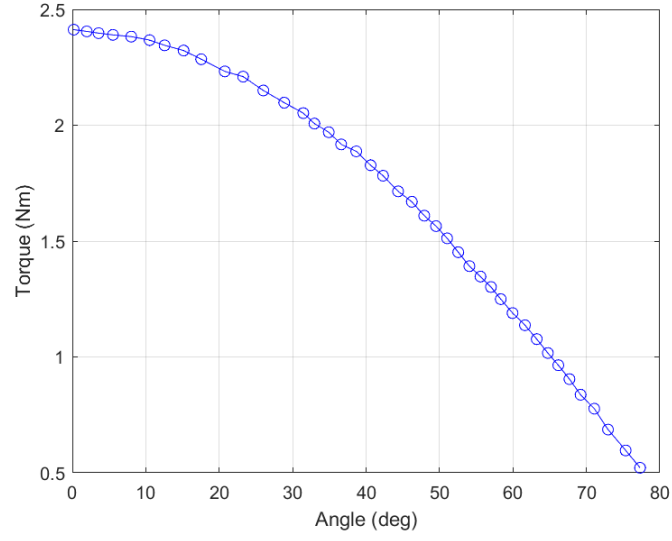


**Figure 5.13:** Torque-angle characteristic curve of 3-phase motor

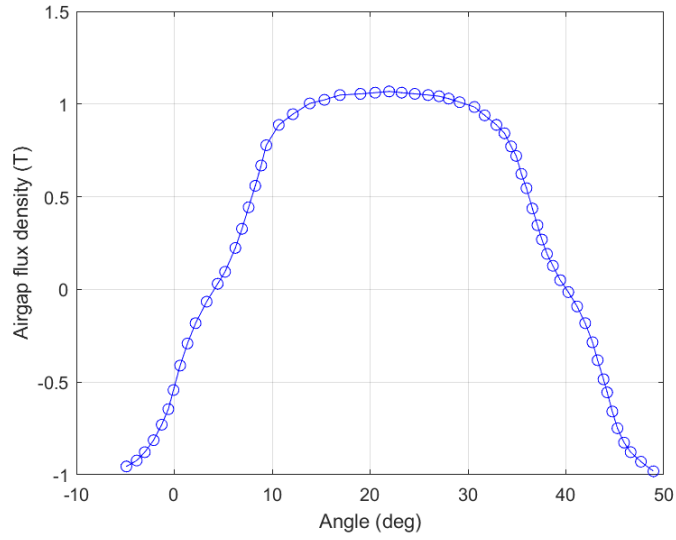


**Figure 5.14:** Air gap flux density of 3-phase motor

Figure 5.13 shows that the peak torque of this 3-phase motor is 2.412Nm in the middle position while rotating 30° in any direction, it can develop 2.075Nm, which equals a reduction of 14%. Regarding the torque density, the above procedure is applied here as well.

$$V_G = \pi \cdot R_{so}^2 \cdot D = \pi \cdot (30mm)^2 \cdot 36mm = 101787mm^3 = 1.0178 \cdot 10^{-4}m^3 \quad (5.8)$$

$$\frac{T_P}{V_P} = \frac{2.412Nm}{1.0178 \cdot 10^{-4}m^3} = 23698 \frac{Nm}{m^3} \quad (5.9)$$

It is obvious that this typology of motor has a much greater torque capability. The peak torque is more than 8 times greater than the one developed by the designed motor, while it is slightly below 5% greater than the peak torque of the motor taken from the previous paper analyzed, even if the volume is 66% smaller. The performances of this motor are better under this aspect as stated by the torque density.

Figure 5.14 presents the air gap flux density characteristic of the 3-phase motor, which is considerably greater than the ones of the other motors presented. This behavior is a confirmation of the greater torque capability of this category of torquers. The distribution has a different period because of the 3-phase excitation applied to the armature windings.

### 5.3 Conclusions

The limited angle torque motor designed in this dissertation project does not match the torque performance required by the suspension system, without exceeding the flux and dimensions limitations. Despite that, the optimization process led to an optimum solution for the geometry of the section, taking into consideration the limited space available to fit the volume of the torquer.

Particle swarm optimization algorithm resulted as a valid and suitable choice for the application, even considering the highly non-linear behavior of the function that relates the geometry of a motor to its torque capability and its many points of local minima, which could have led the algorithm to an erroneous result.

The motor design can still be employed in different applications that do not require great torque and have strict volume limitations.

The MatLab script, shown in Appendix A, can be even more useful because of the parametric design employed and presented in the second chapter of this thesis. This flexibility allows the script to be re-used and adapted for other applications with different specifics and requirements.

# Appendix A

## MatLab scripts

### A.1 Function used to compute peak torque and maximum flux

```
1 function T = BTcalculation(x)
2 g = x(1);
3 lm = x(2);
4 Rsi = x(3);
5 openfemm(1)
6 newdocument(0)
7 smartmesh(1)
8 %% data
9 MC = 1; % distance between windings and PMs
10 wt = g-MC; % windings thickness
11 Rso = 30-wt; %stator_outer_radius (=30mm-windings thickness)
12 theta_R = 120/180*pi;
13 Rri = 5; % rotor inner hole radius
14 h = 1; % distance between end of windings and axis of symmetry
15 Rro = Rsi-g-lm;
16 cd = 3.6; % cd = current density
17 %% stator geometry
18 mi_addnode(Rso,0)
19 mi_addnode(-Rso,0)
20 mi_addnode(Rsi,0)
21 mi_addnode(-Rsi,0)
22 mi_addarc(Rso,0,-Rso,0,180,1)
23 mi_addarc(-Rso,0,Rso,0,180,1)
24 mi_addarc(Rsi,0,-Rsi,0,180,1)
25 mi_addarc(-Rsi,0,Rsi,0,180,1)
26 %% rotor geometry
27 mi_addnode(Rro,0)
```

```

28 mi_addnode(-Rro,0)
29 mi_addarc(Rro,0,-Rro,0,180,1)
30 mi_addarc(-Rro,0,Rro,0,180,1)
31 % inner hole
32 mi_addnode(Rri,0)
33 mi_addnode(-Rri,0)
34 mi_addarc(Rri,0,-Rri,0,180,1)
35 mi_addarc(-Rri,0,Rri,0,180,1)
36 %% windings geometry
37 % outer windings
38 mi_addnode(sqrt(Rso^2-h^2),h)
39 mi_addnode(sqrt(Rso^2-h^2),-h)
40 mi_addnode(-sqrt(Rso^2-h^2),h)
41 mi_addnode(-sqrt(Rso^2-h^2),-h)
42 mi_addnode(sqrt((Rso+wt)^2-h^2),h)
43 mi_addnode(sqrt((Rso+wt)^2-h^2),-h)
44 mi_addnode(-sqrt((Rso+wt)^2-h^2),h)
45 mi_addnode(-sqrt((Rso+wt)^2-h^2),-h)
46 mi_addsegment(sqrt(Rso^2-h^2),h,sqrt((Rso+wt)^2-h^2),h)
47 mi_addsegment(sqrt(Rso^2-h^2),-h,sqrt((Rso+wt)^2-h^2),-h)
48 mi_addsegment(-sqrt(Rso^2-h^2),h,-sqrt((Rso+wt)^2-h^2),h)
49 mi_addsegment(-sqrt(Rso^2-h^2),-h,-sqrt((Rso+wt)^2-h^2),-h)
50 mi_addarc(sqrt((Rso+wt)^2-h^2),h,-sqrt((Rso+wt)^2-h^2),h,180-2*
atan(h/sqrt((Rso+wt)^2-h^2))/pi*180,1)
51 mi_addarc(-sqrt((Rso+wt)^2-h^2),-h,sqrt((Rso+wt)^2-h^2),-h,180-2*
atan(h/sqrt((Rso+wt)^2-h^2))/pi*180,1)
52 % inner windings
53 mi_addnode(sqrt(Rsi^2-h^2),h)
54 mi_addnode(sqrt(Rsi^2-h^2),-h)
55 mi_addnode(-sqrt(Rsi^2-h^2),h)
56 mi_addnode(-sqrt(Rsi^2-h^2),-h)
57 mi_addnode(sqrt((Rsi-wt)^2-h^2),h)
58 mi_addnode(sqrt((Rsi-wt)^2-h^2),-h)
59 mi_addnode(-sqrt((Rsi-wt)^2-h^2),h)
60 mi_addnode(-sqrt((Rsi-wt)^2-h^2),-h)
61 mi_addsegment(sqrt(Rsi^2-h^2),h,sqrt((Rsi-wt)^2-h^2),h)
62 mi_addsegment(sqrt(Rsi^2-h^2),-h,sqrt((Rsi-wt)^2-h^2),-h)
63 mi_addsegment(-sqrt(Rsi^2-h^2),h,-sqrt((Rsi-wt)^2-h^2),h)
64 mi_addsegment(-sqrt(Rsi^2-h^2),-h,-sqrt((Rsi-wt)^2-h^2),-h)
65 mi_addarc(sqrt((Rsi-wt)^2-h^2),h,-sqrt((Rsi-wt)^2-h^2),h,180-2*
atan(h/sqrt((Rsi-wt)^2-h^2))/pi*180,1)
66 mi_addarc(-sqrt((Rsi-wt)^2-h^2),-h,sqrt((Rsi-wt)^2-h^2),-h,180-2*
atan(h/sqrt((Rsi-wt)^2-h^2))/pi*180,1)
67 %% PMs geometry
68 mi_addnode((Rsi-g)*cos(0.5*(pi-theta_R)),(Rsi-g)*sin(0.5*(pi-
theta_R)))
69 mi_addnode(Rro*cos(0.5*(pi-theta_R)),Rro*sin(0.5*(pi-theta_R)))
70 mi_addnode((Rsi-g)*cos(0.5*(pi-theta_R)),-(Rsi-g)*sin(0.5*(pi-
theta_R)))

```

```

71 mi_addnode(Rro*cos(0.5*(pi-theta_R)), -Rro*sin(0.5*(pi-theta_R)))
72 mi_addnode(-(Rsi-g)*cos(0.5*(pi-theta_R)), (Rsi-g)*sin(0.5*(pi-
theta_R)))
73 mi_addnode(-Rro*cos(0.5*(pi-theta_R)), Rro*sin(0.5*(pi-theta_R)))
74 mi_addnode(-(Rsi-g)*cos(0.5*(pi-theta_R)), -(Rsi-g)*sin(0.5*(pi-
theta_R)))
75 mi_addnode(-Rro*cos(0.5*(pi-theta_R)), -Rro*sin(0.5*(pi-theta_R)))
76 mi_addarc((Rsi-g)*cos(0.5*(pi-theta_R)), (Rsi-g)*sin(0.5*(pi-
theta_R)), -(Rsi-g)*cos(0.5*(pi-theta_R)), (Rsi-g)*sin(0.5*(pi-
theta_R)), theta_R/pi*180, 1)
77 mi_addarc(-(Rsi-g)*cos(0.5*(pi-theta_R)), -(Rsi-g)*sin(0.5*(pi-
theta_R)), (Rsi-g)*cos(0.5*(pi-theta_R)), -(Rsi-g)*sin(0.5*(pi-
theta_R)), theta_R/pi*180, 1)
78 mi_addsegment((Rsi-g)*cos(0.5*(pi-theta_R)), (Rsi-g)*sin(0.5*(pi-
theta_R)), Rro*cos(0.5*(pi-theta_R)), Rro*sin(0.5*(pi-theta_R)))
79 mi_addsegment(-(Rsi-g)*cos(0.5*(pi-theta_R)), (Rsi-g)*sin(0.5*(pi-
theta_R)), -Rro*cos(0.5*(pi-theta_R)), Rro*sin(0.5*(pi-theta_R)))
80 mi_addsegment((Rsi-g)*cos(0.5*(pi-theta_R)), -(Rsi-g)*sin(0.5*(pi-
theta_R)), Rro*cos(0.5*(pi-theta_R)), -Rro*sin(0.5*(pi-theta_R)))
81 mi_addsegment(-(Rsi-g)*cos(0.5*(pi-theta_R)), -(Rsi-g)*sin(0.5*(pi-
theta_R)), -Rro*cos(0.5*(pi-theta_R)), -Rro*sin(0.5*(pi-theta_R)))
82 %% air-gap geometry
83 mi_addnode(Rsi-g+MC/3, 0)
84 mi_addnode(-Rsi+g-MC/3, 0)
85 mi_addnode(Rsi-g+2*MC/3, 0)
86 mi_addnode(-Rsi+g-2*MC/3, 0)
87 mi_addarc(Rsi-g+MC/3, 0, -Rsi+g-MC/3, 0, 180, 1)
88 mi_addarc(-Rsi+g-MC/3, 0, Rsi-g+MC/3, 0, 180, 1)
89 mi_addarc(Rsi-g+2*MC/3, 0, -Rsi+g-2*MC/3, 0, 180, 1)
90 mi_addarc(-Rsi+g-2*MC/3, 0, Rsi-g+2*MC/3, 0, 180, 1)
91 %% ratio between inner and outer windings
92 % inner windings surface
93 IW_in_angle = 180-2*asin(h/(Rsi-wt))/pi*180; % angle between
inner windings inner ends and center of the motor.
94 IW_out_angle = 180-2*asin(h/Rsi)/pi*180; % angle between inner
windings outer ends and center of the motor.
95 IW_in_surface = pi*(Rsi-wt)^2*IW_in_angle/360 - sqrt((Rsi-wt)^2-h
^2)*h; % circular segment = circular sector - triangle.
96 IW_out_surface = pi*Rsi^2*IW_out_angle/360 - sqrt(Rsi^2-h^2)*h;
% circular segment = circular sector - triangle.
97 IW_surface = IW_out_surface-IW_in_surface;
98 % outer windings surface
99 OW_in_angle = 180-2*asin(h/Rso)/pi*180; % angle between outer
windings inner ends and center of the motor.
100 OW_out_angle = 180-2*asin(h/(Rso+wt))/pi*180; % angle between
outer windings outer ends and center of the motor.
101 OW_in_surface = pi*Rso^2*OW_in_angle/360 - sqrt(Rso^2-h^2)*h; %
circular segment = circular sector - triangle.

```

```

102 OW_out_surface = pi*(Rso+wt)^2*OW_out_angle/360 - sqrt((Rso+wt)
    ^2-h^2)*h; % circular segment = circular sector - triangle.
103 OW_surface = OW_out_surface-OW_in_surface;
104 IWOW_ratio = IW_surface/OW_surface;
105 %% object properties
106 mi_getmaterial('N35')
107 mi_getmaterial('Air')
108 mi_getmaterial('M-27')
109 mi_addmaterial('25 AWG I+',1,1,0,cd) % inner-lower
110 mi_addmaterial('25 AWG I-',1,1,0,-cd) % inner-upper
111 mi_addmaterial('25 AWG O+',1,1,0,IWOW_ratio*cd) % outer-upper
112 mi_addmaterial('25 AWG O-',1,1,0,-IWOW_ratio*cd) % outer-lower
113 %% block properties
114 mi_addblocklabel(0,0)
115 mi_addblocklabel(Rsi-g-lm/2,0)
116 mi_addblocklabel(Rsi-g+5*MC/6,0)
117 mi_selectlabel(0,0);
118 mi_selectlabel(Rsi-g-lm/2,0);
119 mi_selectlabel(Rsi-g+5*MC/6,0);
120 mi_setblockprop('Air',1,0,'<none>',0,0,1)
121 mi_clearselected
122 mi_addblocklabel(0,Rsi-g-lm/2)
123 mi_addblocklabel(0,-Rsi+g+lm/2)
124 mi_selectlabel(0,Rsi-g-lm/2);
125 mi_setblockprop('N35',1,0,'<none>', 'theta',0,1)
126 mi_clearselected
127 mi_selectlabel(0,-Rsi+g+lm/2);
128 mi_setblockprop('N35',1,0,'<none>', 'theta+180',0,1)
129 mi_clearselected
130 mi_addblocklabel(0,(Rso+Rsi)/2)
131 mi_selectlabel(0,(Rso+Rsi)/2);
132 mi_setblockprop('M-27',1,0,'<none>',0,1,1)
133 mi_clearselected
134 mi_addblocklabel(0,(Rro+Rri)/2)
135 mi_selectlabel(0,(Rro+Rri)/2);
136 mi_setblockprop('M-27',1,0,'<none>',0,2,1)
137 mi_clearselected
138 mi_addblocklabel(0,Rso+(g-MC)/2)
139 mi_selectlabel(0,Rso+(g-MC)/2);
140 mi_setblockprop('25 AWG O+',1,0,'Coil',0,0,0)
141 mi_clearselected
142 mi_addblocklabel(0,-Rso-(g-MC)/2)
143 mi_selectlabel(0,-Rso-(g-MC)/2);
144 mi_setblockprop('25 AWG O-',1,0,'Coil',0,0,0)
145 mi_clearselected
146 mi_addblocklabel(0,Rsi-(g-MC)/2)
147 mi_selectlabel(0,Rsi-(g-MC)/2);
148 mi_setblockprop('25 AWG I-',1,0,'Coil',0,0,0)
149 mi_clearselected

```

```

150 mi_addblocklabel(0,-Rsi+(g-MC)/2)
151 mi_selectlabel(0,-Rsi+(g-MC)/2);
152 mi_setblockprop('25 AWG I+',1,0,'Coil',0,0,0)
153 mi_clearselected
154 mi_addblocklabel(-Rsi+g-MC/2,0)
155 mi_selectlabel(-Rsi+g-MC/2,0);
156 mi_setblockprop('<No Mesh>',1,0,'<none>',0,0,1)
157 mi_clearselected
158 %% air-gap properties
159 mi_selectarcsegment(0,Rsi-g+MC/3);
160 mi_selectarcsegment(0,-Rsi+g-MC/3);
161 mi_selectarcsegment(0,Rsi-g+2*MC/3);
162 mi_selectarcsegment(0,-Rsi+g-2*MC/3);
163 mi_setarcsegmentprop(0,'periodic air gap',0,0)
164 mi_clearselected
165 %% unbounded domain
166 mi_makeABC(7,100,0,0,0)
167 mi_addblocklabel(50,50)
168 mi_selectlabel(50,50);
169 mi_setblockprop('Air',1,0,'<none>',0,0,1)
170 %% problem commands
171 mi_probdef(0,'millimeters','planar',1e-8,1000,30,0)
172 mi_saveas('LATM.fem')
173 mi_createmesh;
174 %% post processor
175 mi_addboundprop('periodic air gap',0,0,0,0,0,0,0,0,6,0,0)
176 mi_analyze(1)
177 mi_loadsolution
178 %% torque computation at 0 degrees
179 mo_selectblock(0,(Rsi-g-lm+Rri)/2)
180 mo_selectblock(0,-Rsi+g+lm/2)
181 mo_selectblock(0,Rsi-g-lm/2)
182 T = -mo_blockintegral(22);
183 %% flux computation at 0 degrees
184 mi_modifyboundprop('periodic air gap',10,30)
185 betaR = linspace(10,50,30)/180*pi;
186 mo_seteditmode('contour')
187 % rotor flux
188 for i=1:length(betaR)
189     mo_addcontour(Rri*cos(betaR(i)),Rri*sin(betaR(i)))
190     mo_addcontour(Rro*cos(betaR(i)),Rro*sin(betaR(i)))
191     Br = mo_lineintegral(0); % gives back a total flux and
average flux respectively
192     mo_clearcontour
193     BR0(i) = Br(2); % considering only the second component
194 end
195 BrMAX = max(BR0);
196 % stator flux
197 betaS = linspace(0,90,60)/180*pi;

```

```

198     for i=1:length(betaS)
199         mo_addcontour(Rsi*cos(betaS(i)),Rsi*sin(betaS(i)))
200         mo_addcontour(Rso*cos(betaS(i)),Rso*sin(betaS(i)))
201         Bs = mo_lineintegral(0); % gives back a total flux and
average flux respectively
202         mo_clearcontour
203         BS0(i) = Bs(2);
204     end
205     BsMAX = -min(BS0); % use min (instead of max) cause flux is
negative on the right side of the stator in this configuration
206     if BsMAX > 1.2 || BrMAX > 1.4
207         T = 0;
208     end

```

## A.2 Optimization of the parameters with particle swarm algorithm

```

1     close all
2     clear all
3     clc
4     options = optimoptions('particleswarm');
5         options.Display = 'iter';
6         options.FunctionTolerance = 1e-3;
7         options.SwarmSize = 10;
8     nvars = 3; % g,lm,Rsi
9     lb = [4,2.5,18];
10    ub = [6,4,22];
11    x = particleswarm(@(x)BTcalculation(x),nvars,lb,ub,options)

```

# Bibliography

- [1] *A Survey on Passive, Active and Semiactive Automotive Suspension Systems and Analyzing Tradeoffs in Design of Suspension Systems*. Hubli, India, 2018, pp. 2908–2913 (cit. on p. 1).
- [2] *A Survey On Comparison Of Electric Motor Types And Drives Used For Electric Vehicles*. Antalya, Turkey, Sept. 2014, pp. 218–223 (cit. on p. 7).
- [3] Z. Cao, A. Mahmoudi, S. Kahourzade, and W.L. Soong. «An Overview of Electric Motors for Electric Vehicles». In: (Sept. 2021), pp. 1–6 (cit. on p. 7).
- [4] *Understanding of induction motors made easy*. Toronto, ON, Canada, Sept. 2011, pp. 1–6 (cit. on p. 12).
- [5] R. Nasiri-Zarandi, M. Mirsalim, and A. Cavagnino. «Analysis, Optimization, and Prototyping of a Brushless DC Limited-Angle Torque-Motor With Segmented Rotor Pole Tip Structure». In: *IEEE Transactions On Industrial Electronics* 62 (Aug. 2015), pp. 4985–4993 (cit. on pp. 17, 31, 55, 57).
- [6] P. Hekmati and M. Mirsalim. «Design and Analysis of a Novel Axial-Flux Slotless Limited-Angle Torque Motor With Trapezoidal Cross Section for the Stator». In: *IEEE Transactions On Energy Conversion* 28 (Dec. 2013), pp. 815–822 (cit. on p. 17).
- [7] *Brushless d.c Limited Angle Torque Motor*. New Delhi, India, Aug. 2002, pp. 511–516 (cit. on p. 18).
- [8] S.L.Chen, N.Kamaldin, T.J.Teo, W.Liang, C.S.Teo, G.Yang, and K.K.Tan. «Toward Comprehensive Modeling and Large-Angle Tracking Control of a Limited-Angle Torque Actuator With Cylindrical Halbach». In: *IEEE/ASME Transactions On Mechatronics* 21 (Feb. 2016), pp. 431–442 (cit. on p. 19).
- [9] D. Meeker. URL: <https://www.femm.info/wiki/HomePage/backlinks> (cit. on p. 21).
- [10] C.-C. Tsai, S.-C. Lin, H.-C. Huang, and Y.-M. Cheng. «Design and control of a brushless DC limited-angle torque motor with its application to fuel control of small-scale gas turbine engines». In: *Mechatronics* 19 (2009), pp. 29–41 (cit. on p. 24).

- [11] G. Volpe, M. Popescu, I. Foley, and J. Goss. «Development of non-oriented and grain-oriented silicon steel». In: *IEEE Transactions on Magnetics* 21 (Sept. 1985), pp. 1903–1908 (cit. on p. 27).
- [12] *Winding Material Effect on High Speed Brushless Permanent Magnet Machines*. Baltimore, MD, USA, Sept. 2019, pp. 3144–3149 (cit. on p. 28).
- [13] Iowa State University, Center for Nondestructive Evaluation. URL: <https://www.nde-ed.org/Physics/Magnetism/HysteresisLoop.xhtml> (cit. on p. 36).
- [14] *Unconstrained global optimization: A benchmark comparison of population-based algorithms*. Colmar, France, Mar. 2015, pp. 230–237 (cit. on p. 41).
- [15] *A Review of Population-Based Optimization Algorithms*. Ayobo, Nigeria, Mar. 2020, pp. 1–7 (cit. on p. 43).
- [16] *Particle swarm arrows animation*. Jan. 2017. URL: <https://commons.wikimedia.org/w/index.php?curid=54975083> (cit. on p. 47).
- [17] R. Galluzzi. *3-Phase Motor Design Report*. Tech. rep. MA: Digital Equipment Corporation, Mar. 2021 (cit. on p. 59).